MICROWAVE CHARACTERIZATION OF VERTICAL CAVITY SURFACE EMITTING DIODE LASER AND TRANSISTOR LASER

BY

CURTIS YILIN WANG

DISSERTATION

Submitted in partial fulfillment of the requirements
for the degree of Doctor of Philosophy in Electrical and Computer Engineering
in the Graduate College of the
University of Illinois at Urbana-Champaign, 2018

Urbana, Illinois

Doctoral Committee:

Professor Milton Feng, Chair
Professor Jianming Jin
Associate Professor John M. Dallesasse
Assistant Professor Peter Dragic

ABSTRACT

Semiconductor lasers are widely deployed in optical transceivers for optical fiber based short-reach (< 100m) data links. With increasingly growing data traffic worldwide in data centers, developments of faster optical transceivers, hence high-speed semiconductor lasers, are highly demanded.

The vertical cavity surface-emitting laser (VCSEL) is the most commercially popular choice. With high reflectivity DBR mirrors and oxide-confinement for emission mode control and leakage current reduction, VCSELs are able to achieve a low laser threshold and high modulation bandwidth. Currently in published research results, the highest data transmission rate demonstrated for an 850 nm VCSEL is 57 Gb/s error-free at 25 °C and 50 Gb/s error-free at 85 °C. Nevertheless, the bandwidth and data transmission performance of diode lasers, such as VCSELs, are fundamentally limited by the slow spontaneous recombination lifetime. Therefore, a new kind of semiconductor laser, the transistor laser (TL), is proposed to break the bandwidth bottleneck as the dynamic carrier transport in the base of a TL drastically reduces the spontaneous recombination lifetime.

Ultimately to reach low threshold and high energy per bit efficiency, the first oxide-confined vertical cavity transistor laser (VCTL) is realized with a trench oxidation process and a lateral-feeding base metal design. To further reduce the excessive emitter series resistance, a VCTL with partially etched mesa is developed and fabricated. The tunneling modulation aspect and possible application of the TL is also explored in this dissertation.

ACKNOWLEDGMENTS

First, I would like to thank my advisor, Professor Milton Feng, for his guidance and support. In addition, I also thank Professor Nick Holonyak, Jr. for his inspiration. It is my upmost honor and pleasure to have the opportunity to work with such a brilliant innovator. Second, I would like to express my gratitude to our previous HSIC group members: Dr. Michael Liu, Dr. Mong-Kai Wu, Dr. Rohan Bambery, Dr. Fei Tan, Dr. Huiming Xu, and Dr. Eric Iverson for the immense help and insightful conversations. I would especially like to thank Dr. Rohan Bambery and Dr. Fei Tan for serving as my mentors as well as great role models for hard work, effective time management and endeavor; without the foundation built and the skill sets they taught me, the work in this dissertation would not be possible. Furthermore, I would like to thank Dr. Michael Liu for the collaboration on high-speed VCSEL and most importantly for his friendship. I would also like to thank all the current HSIC group members for their tremendous help and discussions. I would like to thank Mr. Junyi Qiu for his help on device modeling and Mr. Hsiao-Lun Wang for his diligence on following the VCTL fabrication process. It has been a real pleasure to work with you all. In addition, I would like to thank my wife Dr. Wan-Yi, Amy, Chu for her support and companionship. Finally, I would like to thank all my family and friends for the time and experiences we shared together. These people are what make me whole.

To My Dear Wife and Family

TABLE OF CONTENTS

1. INTRODUCTION

For semiconductor devices, the carrier recombination is a key process that cannot be neglected. The minority carrier recombination led Bardeen and Brattain to the discovery of the first bipolar junction transistor (BJT) [1] and further improvement in carrier confinement in the base of the transistor resulted in the development of heterojunction bipolar transistor (HBT). When translated to semiconductor light emitting devices, the radiative recombination generates the photon light output. The semiconductor coherent light emission was realized in 1962, the diode lasers (DLs) were first demonstrated by General Electrics (GE) researchers; Hall with an infrared emission at 840 nm [2] and Holonyak with a visible emission at 710 nm [3]. Further advanced developments such as single and double heterojunction confinement [4, 5], quantum well active region [6, 7], oxide confinement [8-10] and DBR mirror cavity [11] established the fundamentals for the development of the first low threshold vertical cavity surface emitting laser (VCSEL) [12].

Optical modulation bandwidth for a semiconductor laser is fundamentally governed by the thermally limited spontaneous radiative recombination lifetime, τ_{rec}, photon lifetime, τ_p, and cavity photon density. The radiative recombination lifetime of electron-hole pairs in quantum wells (QWs) can be considered as an electrical delay and the photon lifetime inside the cavity can be treated as an optical delay which limits the frequency response of a diode laser. Thus, it is important to accurately determine the device lifetimes, especially τ_{rec}, in order to further improve the bandwidth of a directly modulated laser (DML).

Although a diode laser, such as a VCSEL, has a relatively high modulation bandwidth, it is limited by the τ_{rec} imposed by the diode structure.

In 2004, the radiative recombination in the base of a HBT as an output signal was realized; thus, the three-port light-emitting transistor was invented [13]. Furthermore, with the insertion of quantum wells (QWs) in the base and employing the optical cavity, the transistor demonstrated the laser operation in the active mode – the transistor laser (TL) [14, 15]. Because of the tilted charge profile in the base, the recombination lifetime is greatly reduced compared to diode lasers [16]. The reduced recombination lifetime can improve the intrinsic optical modulation bandwidth of the device and reduce the resonance peak amplitude which are important high-speed characteristics. With top and bottom AlGaAs DBR mirrors, the first vertical cavity transistor laser (VCTL) was realized in 2012 [17]. A bandwidth of 11.1 GHz was achieved an oxide-confined VCTL [18]; nevertheless, the speed potential of VCTL is limited by the electrical parasitics induced by the large device layout. Therefore, by optimizing the device layout, it is expected that VCTL will break the bandwidth bottleneck of VCSEL.

The goal of our research is to develop microwave characterization techniques for determining semiconductor laser extrinsic and intrinsic parameters and apply such techniques to develop, fabricate and characterize next-generation high-speed oxide-confined VCTLs**.**

1.1 Outline of Problem

As the data traffic and capacity in the data centers continue to grow with popularized handheld devices and other on-line services such as video streaming and cloud computing, high-speed and energy-efficient short-reach data links are in high demands. Cisco has projected data traffic from 2015 to 2020 with a compound annual growth rate (CAGR) of 27% to over 15 zettabytes per year in 2020, and the traffic within the data centers accounts for over 75% of the total data traffic [19]. The signal integrity of electrical interconnects suffers greatly from skin effect at high-speed data traffic and is impeded by crosstalk between the neighboring channels. Thus, high-speed optical links are used in the short-reach data transmissions in the data centers because of their high bandwidth and low loss capability and immunity to electromagnetic crosstalk between channels. Currently, two majority products are widely deployed in data centers: (1) multimode optical fiber (MMF) links based on directly modulated 850 nm oxide-confined VCSELs and (2) single-mode optical fiber (SMF) links based on silicon photonics based transceivers. Both technologies are able to meet the market demands; nevertheless there are fundamental limitations that prevent advancement beyond the current performance. VCSEL-based optical links are popular due to the relative ease of fabricating high-speed multimode VCSELs and photo-detectors (PDs) from GaAs epitaxial structures and the alignment tolerance of a packaged multimode transceiver is an order of magnitude larger than to its single mode counterpart [20]. Furthermore, MMF links implement direct modulation on the VCSELs, resulting in significantly less power consumption, given the same optical modulation amplitude (OMA), due to the low laser threshold and the lack of external

modulators. Nevertheless, the nature of MMF limits the channel per fiber, optical data density, to 1 and the effective distance, typically < 300 m, due the chromatic dispersion and attenuation.

As the name suggests, silicon (Si) photonics adopts the standard silicon process and hence a wide variety of optical components, such as filters, resonators and isolators, are readily deployed. Silicon photonics based optical transceivers typically utilize an InP continuous wave (CW) single-mode distributed feedback (DFB) laser as source, external modulators, such as Mach-Zehnder modulator, and wavelength division multiplexers (WDMs) [21]. The single-mode nature of the laser source allows the implementation of WDMs to increase the density of data per optical channel. However, the power consumption, as mentioned, is large due to the integration of many active components other than the laser source and the packaging cost is higher for the more complex design. Furthermore, the Si photonics designs are not easily scalable due to the size restrictions of the optical components.

The current standard of optical channel rate ranges from 10 Gb/s to 25 Gb/s and has been projected that the next-generation would require 50 Gb/s per channel. Fundamentally, to improve the data rate of the optical transceivers, the bandwidth performance of the laser source needs to be enhanced. All semiconductor lasers on the market are diode lasers (DLs) which have fundamental bandwidth limitations because of the carrier dynamics in the active region. The carriers accumulate in the quantum wells and wait to recombine, resulting in a slow recombination lifetime on average. The nanosecond recombination lifetime not only limits the modulation bandwidth but also leads to a large

resonance peak in the frequency response due to the relaxation oscillation at low bias current. The resonance peak is associated with inter-symbol interference and hence poor signal integrity. On the other hand, within a TL, hole and electron transport in the base are established by fast processes governed by dielectric relaxation time and submicron base diffusion transit time, both in picoseconds rather than nanoseconds as in DLs [16, 22]. The reduced recombination lifetime not only improves the optical modulation but also relieves the resonance bump. Hence, TLs are promising devices to break through the fundamental limitations of DLs and achieve a higher modulation bandwidth. Furhermore, the base-collector junction offers revolutionary intra-cavity photon-assisted tunneling (ICpaT) that opens the possibility of tunneling modulation, under speed of femtoseconds, and compact and scalable photonics integrated circuits. Combining the dynamic and scalable features of TLs and the strong confinement of a high-Q vertical cavity, the VCTL is expected to achieve low threshold and high modulation bandwidth and be implemented to achieve optical transceivers with data rate above 50 Gb/s and 100Gb/s.

1.2 Organization of Work

The organization of the dissertation is as follows:

Chapters 2 and 3 present the up-to-date research results for the microwave characterization techniques, performed on state-of-the-art VCSEL and development of next-generation high-speed oxide-confined VCTL.

In Chapter 2, we present data of a high-speed 850 nm VCSEL with 5 μm aperture and a threshold of 0.8 mA at room temperature (RT). The device is capable of achieving

57 Gb/s error-free data transmission with an energy/data efficiency of 431 fJ/bit at RT and 50 Gb/s error-free data transmission with an energy/data efficiency of 456 fJ/bit at 85 °C [23, 24]. We apply the microwave de-embedding technique that is used to determine the extrinsic parasitic parameters and the intrinsic recombination and photon lifetime of the VCSEL. The extracted intrinsic bandwidth, recombination and photon lifetime of the VCSEL is ~30 GHz, ns, and ps at RT and is ~27 GHz, ns, and ps at 85 °C.

In Chapter 3, we outline the development of 980 nm VCTL with oxide confinement and lateral-feeding design to eliminate the undesired radiative recombination underneath the emitter contact. The VCTL can only show laser operation below -45 °C because of the mismatch between the DBR design and the QW emission. VCTL is able to achieve a 2.4 mA threshold and a bandwidth of 11.1 GHz at 80K. Data, such as L-I-V family curves, laser spectra, and optical response, is further analyzed to identify that the large series emitter resistance is hindering the bandwidth potential of VCTLs. Subsequently, process development on partially etching the top DBR mesa to reduce the emitter resistance is presented. The fabricated partially etched VCTL then goes through the same characterizations and a microwave parasitic equivalent model is built for further analysis.

In Chapter 4, we outline and explore the electron and photon interaction within the cavity at the base-collector junction of the TL. We observed a unique photon-assisted tunneling (PAT) process for electrons within the cavity, hence the name intra-cavity photon-assisted tunneling (ICpaT). Different from regular PAT, not only is the light output affected by ICpaT, the electrical current output of the TL is altered. The physics of ICpaT is illustrated and the possible applications are explored.

2. FROM HIGH-SPEED VERTICAL SURFACE EMITTING LASER (VCSEL) TO VERTICAL CAVITY TRANSISTOR LASER

Development of oxide-confined VCSELs has been growing to meet the recent surging demands of the data traffic because of their low threshold and high modulation bandwidth capability. The oxide-confined VCSELs utilize a lateral oxidation process to form oxide apertures which not only provide electrical current confinement but also optical confinement due to the high refractive index contrast [8, 12]. Currently, transceivers based on 25-28 Gb/s 850 nm VCSELs are already commercialized for 100 Gb/s optical transceivers. As for device research, single VCSLE speed performance above 50 Gb/s has been demonstrated by three major academic research institutes: Chalmers University (Sweden) [25], TU-Berlin (Germany) [26], and UIUC [23].

To further improve the speed performance, a microwave technique of characterizing the VCSELs required development to extract both the extrinsic and intrinsic parameters to accurately determine what the limiting factors are of the current VCSELs. A small signal circuit model of a high-speed VCSEL has been developed to de-embed the extrinsic parasitic and obtain the intrinsic laser response. Hence, the recombination and photon lifetime can be extracted by fitting the intrinsic optical response.

2.1 Principles and Characteristics of VCSEL

The general epitaxial structure of an 850 nm VCSEL includes top and bottom DBR mirrors made of $Al_xGa_{1-x}As$ with a quantum well (MQW) active region intermediated between them. The laser principle of VCSEL is no different than other kinds of

semiconductor lasers. The peak wavelength of the gain spectrum, provided by the MQW active region, should match the resonant wavelength of the DBR cavity and the round-trip phase condition is given by

$$\frac{4\pi nL}{\lambda} + \varphi_1 + \varphi_2 = 2m\pi, \tag{2.1}$$

where n is the refractive index of the QW active region, L is the cavity length, λ is the resonance emission wavelength, φ_1 and φ_2 are the phase delays of the alternating DBR layers and m is any positive integer that ensures the round-trip 2π phase shift.

The laser gain threshold condition is governed by Eqn. 2.2 and 2.3,

$$\Gamma g_{th} = \alpha_i + \alpha_m, \tag{2.2}$$

$$\alpha_m = \frac{1}{2L}\ln(\frac{1}{R_1 R_2}), \tag{2.3}$$

where Γ is the optical confinement factor, g_{th} is the threshold gain, α_i is the intrinsic material loss, and α_m is the mirror loss, which can be writen in terms of L, R_1 and R_2, the DBR mirror reflectivity. Different from an edge-emitter stripe laser, the high reflectivity of the DBR mirrors, > 99.5 %, allows short cavity design. Therefore, VCSELs can achieve low threshold and high bandwidth.

Since VCSEL is an electrically pumped laser, the laser threshold is characterized by a threshold current. Figure 2.1 shows the temperature-dependent light output power and input current, *L-I*, curves of a high-speed UIUC VCSEL, from RT to 85 °C. The detailed epitaxial layer structure of the VCSEL is shown in [22].

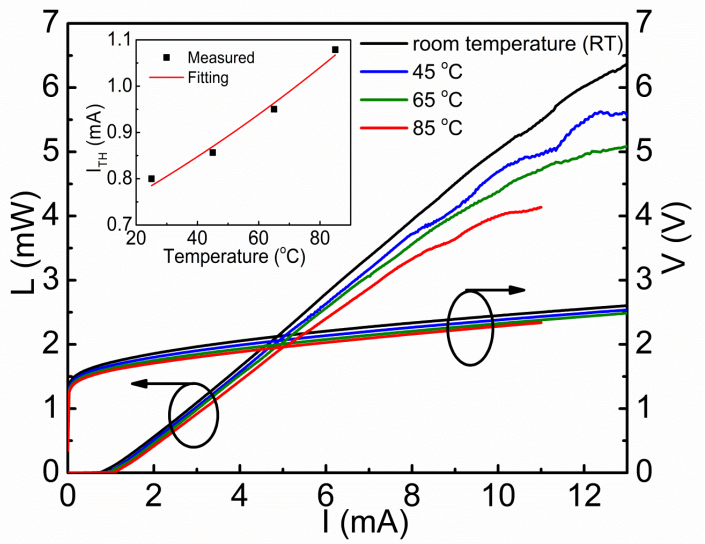

Figure 2.1. L-I-V characteristics of the 850 nm oxide-confined VCSEL from room temperature (~25 ˚C) to 85 ˚C. The inset shows the measured data and fitting of the threshold current versus temperature to obtain I_o = 0.69 mA and T_o = 195 ˚C, under the assumption that $F(T,\Delta\lambda)=1$.

The threshold current increases from I_{TH} = 0.8 mA at 25 °C to 0.86 mA at 45 °C, to 0.95 mA at 65 °C, and eventually to 1.08 mA at 85 °C. The VCSEL threshold current (I_{TH}) as a function of the temperature (T) can be modeled by the following empirical formula [27],

$$I_{TH}(T)=F(T,\Delta\lambda)\cdot I_{TH}^{EEL}=F(T,\Delta\lambda)\cdot I_{0}\cdot\exp\left(T/T_{0}\right), \tag{2.4}$$

where $I_{TH}^{EEL}(T)$ describes the edge-emitter like behavior, exponential fitting, and $F(T,\Delta\lambda)$ is the factor that accounts for the gain-cavity wavelength detuning resulted from the narrow resonance emission wavelength range of the top DBR mirror stacks. We assumed the detuning factor $F(T,\Delta\lambda)=1$ since the VCSEL MQW emission spectrum is closely match with that of the DBR mirror cavity [28]. The fitted data of the threshold current with respect to temperature for the VCSEL is shown in the inset of Figure 2.1, and the fitted 0 °C threshold current and characteristics temperature are I_o = 0.69 mA and T_o = 195 °C

respectively. Derived from the slope of the *L-I* curves, the slope efficiency of the device is ~ 0.58 W/A at room temperature and ~0.5 W/A at 85 °C. the slope efficiency is correlated to the differential gain of the VCSEL, which is one of parameters that affect the bandwidth

The DBR mirror cavity provides the longitudinal confinement. Furthermore, there are also transverse modes for laser coherent emission. Unconfined transverse modes increase the number of emission modes that need to be supported by the input current and hence resulting in higher threshold current. The oxide aperture provides a native transverse mode confinement. Above the active region, there is a high-Al content layer which can be laterally oxidized, Al_xO_y, to form an oxide aperture for electrical and optical confinement. Furthermore, the oxide aperture diameter of the VCSEL can be scaled with the control of the oxidation depth from the DBR mesa peripheral into the center of the VCSEL. Figure 2.2 shows the optical spectrum of the device under the bias of I = 2.5 mA (25 °C) and I = 3.6 mA (85 °C). The biasing points correspond to a ratio of $I/I_{TH} \sim 3$ for the respective ambient temperatures. A redshift of 3.98 nm is observed when the bias and temperature condition changes. From the optical mode spacing, $\lambda(1,1) - \lambda(2,1) = 0.86\,\text{nm}$ at room temperature, the optical modal diameter, d_o, of the device can be determined to be ~5 μm by solving the Helmholtz equation shown in Eqn. 2.5 [28],

$$k_o^2(2,1) - k_o^2(1,1) = \left[\frac{2\pi}{\lambda(2,1)}\right]^2 - \left[\frac{2\pi}{\lambda(1,1)}\right]^2 = \frac{3\pi^2}{\tilde{n}^2 d_o^2}, \tag{2.5}$$

where λ(1,1) and λ(2,1) are fundamental wavelength and the first high-order mode wavelength and $\tilde{n}$ = 3.3 is the refractive index of the high-Al content $Al_xGa_{1-x}As$ layer at λ = 850 nm inside the aperture.

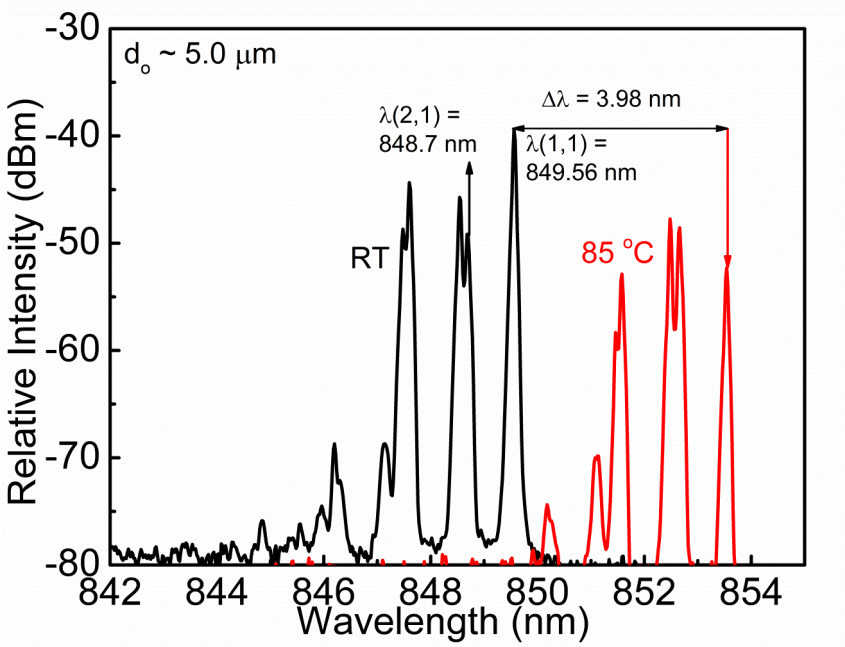

Figure 2.2. Optical spectrum of the 850 nm oxide-confined VCSEL at two biasing and temperature conditions: the black curve represents room temperature measurement at I = 2.5 mA ($I/I_{th} \sim 3$) and the red curve represents 85 ˚C measurement at I = 3.6 mA ($I/I_{th} \sim 3$). The optical aperture is determined to be 5 μm.

A lower laser threshold can be achieved by further scaling down the aperture size and suppressing the higher-order modes. It has been demonstrated by scaling down the aperture size to 2 μm, a single mode like operation, side mode suppression (SMSR) of 36.2 dB, is observed and the laser threshold is reduced down to 0.14 mA. Figure 2.3 shows the optical spectrum of the small aperture VCSEL [28].

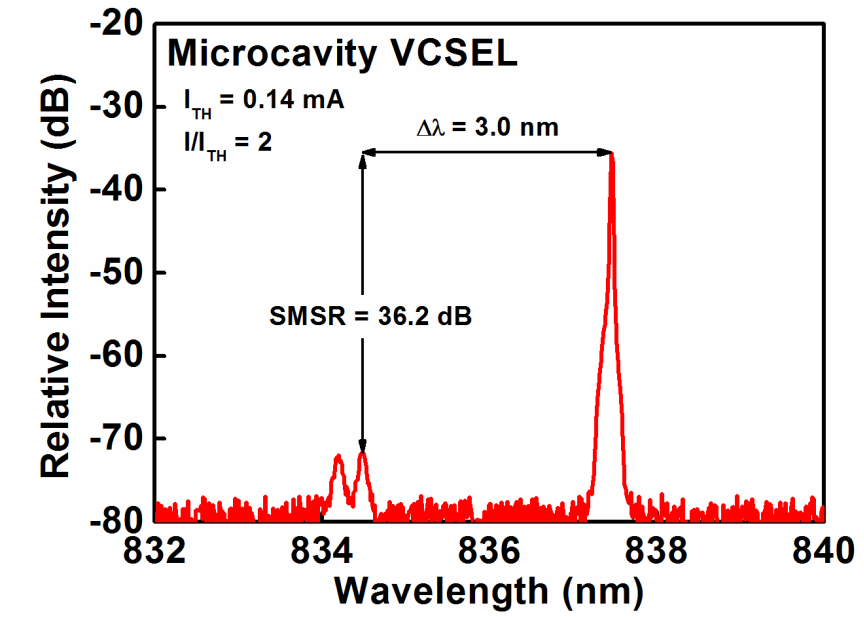

Figure 2.3. The spectrum of the 2 μm aperture VCSEL with threshold current I_{TH} = 0.14 mA biased at I = 0.28 mA. The small aperture allows less high-order modes in the gain profile.

It has also been demonstrated by scaling down the aperture of the VCSEL, the bandwidth of the device also increases. This is due the reduction of parasitic capacitance, $C = \varepsilon A/d$, and hence decreasing parasitic delay. However, excessive scaling down of the aperture can affect the data transmission performance. The optical power might not provide enough optical modulation amplitude and the high resistance of the small cavity VCSEL results in impedance mismatch to the standard 50 Ω of electronics.

2.2 Method of Extracting Intrinsic Optical Response and Data Transmission Performance

In order to accurately represent the VCSEL and de-embed the electrical parasitic, a physical model is needed as the basis for the equivalent circuit model. Previously we have constructed a physical schematic of microcavity VCSEL to model the electrical parasitic parameters [28]. A modified version of the physical schematic for the improved epitaxial structure is shown in Figure 2.4 [22]. The physical meaning of each parameter is described in the annotation of Figure 2.4.

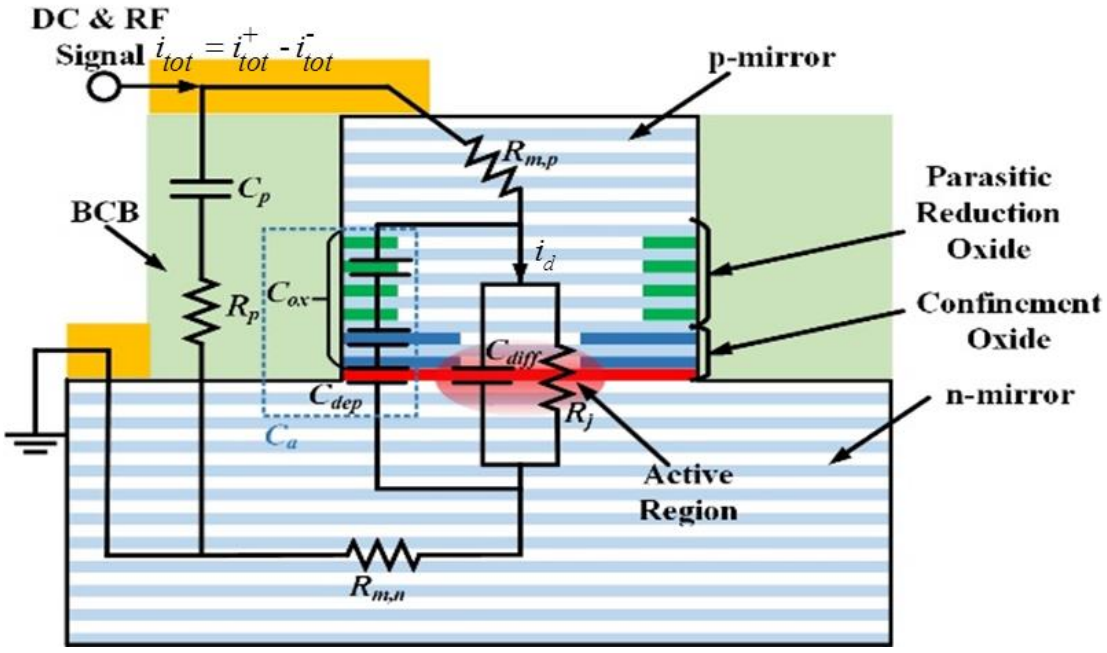

Figure 2.4. Physical model with equivalent circuit including the parasitic parameter identified as follows: C_p and R_p, the p-pad capacitance and resistance; $R_{m,p}$ and $R_{m,n}$, the p-DBR and n-DBR mirror series resistance; C_{diff}, diffusion capacitance at the active region; R_j, junction resistance at the active region; C_{ox} and C_{dep}, the lumped oxide capacitance and depletion capacitance. C_a is the total parasitic capacitance resulted from C_{ox} and $C_{dep.}$

Regarding the two port S-parameter theory, if the mirror resistance is partially attributed to terminate the output port, the reflection coefficient, $\Gamma(f)$, is equivalent to $S_{11}(f)$ and can be expressed as,

$$\Gamma(f) = S_{11} = \frac{i_{tot}^{-}(f)}{i_{tot}^{+}(f)} = \frac{i_{tot}^{+}(f) - i_{tot}(f)}{i_{tot}^{+}(f)}, \tag{2.6}$$

where $i_{tot}^{+}(f)$ is the transmitted modulation current wave and $i_{tot}^{-}(f)$ is the reflected modulation current wave. The total modulation current injected to the VCSEL at frequency f can be defined as $i_{tot}(f) = i_{tot}^{+}(f) - i_{tot}^{-}(f)$ at the input node. The electrical parasitic transfer function can be expressed as,

$$H_{par}(f) = \frac{i_d(f)}{i_{tot}^{+}(f)} = \frac{i_d(f)}{i_{tot}(f)} \cdot (1 - S_{11}), \tag{2.7}$$

where $i_d(f)$ is the portion of the transmitted small signal modulation current that goes through the VCSEL intrinsic active region. By fitting both the magnitude and the phase of the $S_{11}(f)$ measurement data, the electrical parasitic parameters can be extracted and be used to formulate the electrical parasitic transfer function. Figure 2.5 (a) and (b) shows that the modeled $S_{11}(f)$ results are well fitted with the measurement data at various biasing points at both RT and 85 °C. The fitted electrical parasitic parameters are summarized in Table A.1.

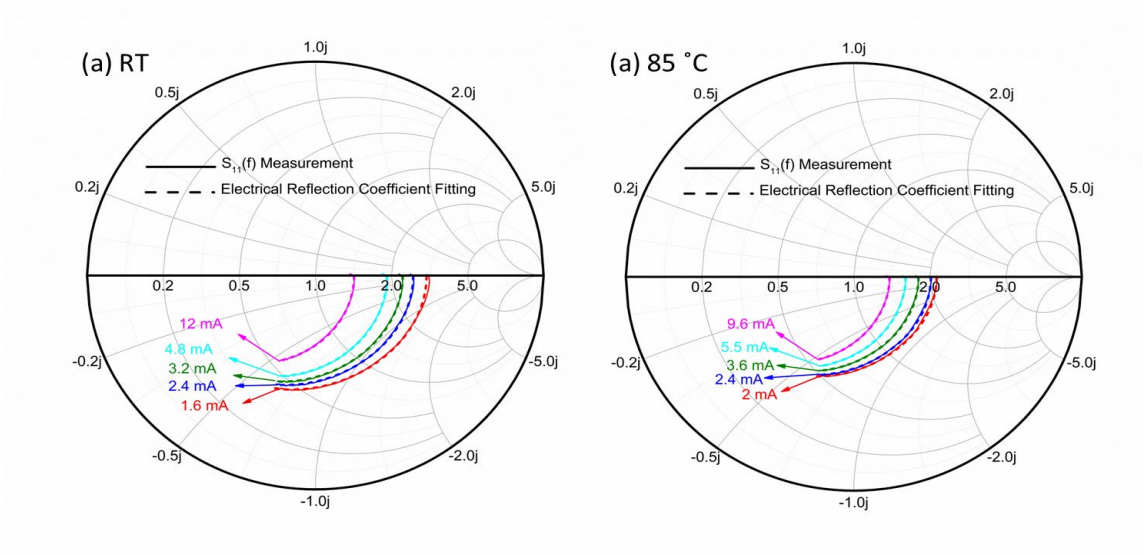

Figure 2.5. Measurement $S_{11}(f)$ data and fitting of the electrical reflection coefficient of the 5 μm optical aperture VCSEL at both RT and 85 ˚C. The fitting curves are generated from the equivalent circuit shown in Figure 2.4.

One way to verify the accuracy of the fitting parameter is to compare the fitted DBR mirror resistance to the derived differential resistance from the *I-V* curves in Figure 2.1. The DBR mirror resistance is the most dominant resistance element since an ideal diode should intrinsically have very low resistance after turn on, especially at higher biasing current. The differential resistances at various biasing points are summarized in Table A.1 as well.

The optical microwave small signal characterization is performed on the VCSEL using an Agilent 50 GHz Parametric Network Analyzer (PNA) with two-port calibration. The electrical microwave signal from port 1 of the PNA is combined with the DC bias through an Agilent 50 GHz bias Tee, and the coupled optical output is relayed into a New Focus 25 GHz Photodetector. The converted electrical signal is fed into port 2 of the PNA. Therefore, the optical modulation response data, $S_{21,\text{data}}(f)$, obtained from the PNA,

consists of the following superimposed microwave responses: photodetector module transfer function, $H_{PD}(f)$, laser intrinsic optical response, $S_{21,\text{int}}(f)$, and electrical parasitic transfer function, $H_{par}(f)$. The relationship of these three responses and the measurement data can be expressed as,

$$dB(S_{21,data}(f)) = dB(H_{PD}(f)) + dB(S_{21,\text{int}}(f)) + dB(H_{par}(f)). \quad (2.8)$$

In order to extract the laser intrinsic optical response, $S_{21,\text{int}}(f)$, $H_{PD}(f)$ and $H_{par}(f)$ need to be de-embedded out of measured $S_{21,\text{data}}(f)$ as inferred from Eqn. 2.8.

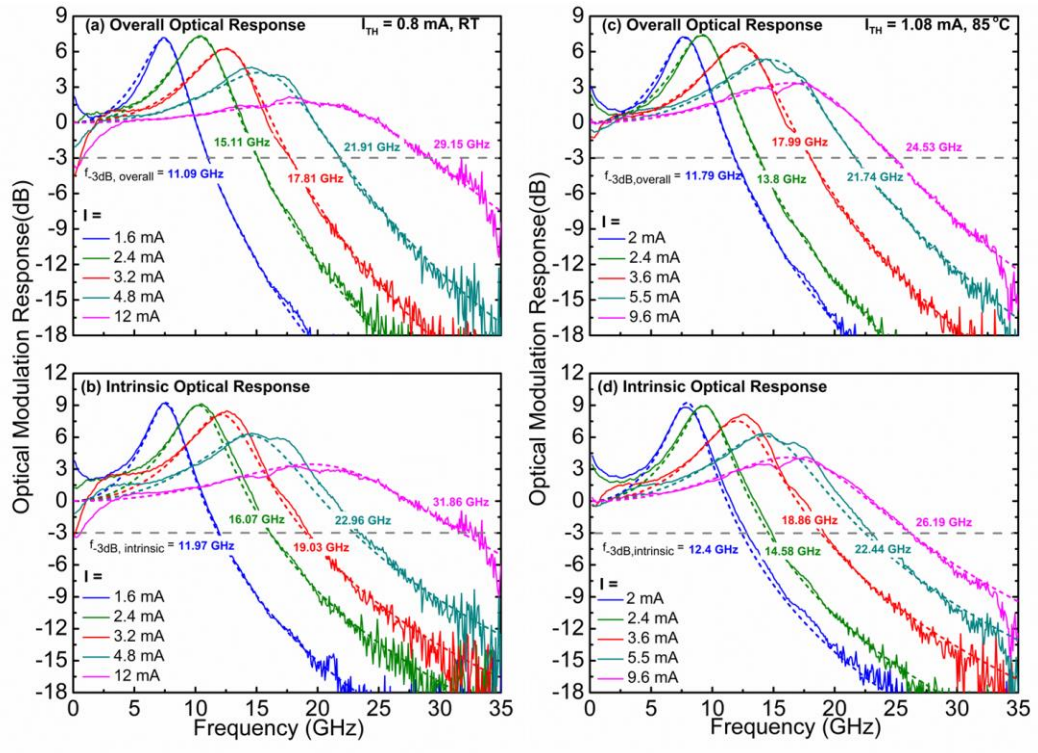

Figure 2.6. (a) & (c) The overall optical frequency response of the 5 μm optical aperture VCSEL at RT and 85 °C. (b) & (d) The intrinsic optical response of the 5 μm optical aperture VCSEL. The highest –3 dB modulation bandwidth of the overall optical response is 29.15 GHz and 24.53 GHz at RT and 85 °C whereas it is 31.86 GHz and 26.19 GHz for the intrinsic optical response at RT and 85 °C.

It is well verified that by solving the Statz and deMars rate equation [29], the laser intrinsic transfer function can be obtained as follows,

$$S_{21,\text{int}}(f) = \frac{A}{1 - f^2 / f_R^2 + j(f/2\pi f_R^2)\gamma}, \tag{2.9}$$

where A is magnitude fitting parameter, f_R, is the resonance frequency and γ is the damping rate of the optical modulation response. The intrinsic laser optical response, $S_{21,\text{int}}(f)$, can be fitted with Eqn. 2.7 by de-embedding measured $S_{21,\text{data}}(f)$ at various biasing current points over the frequency range of 0.1 to 35 GHz. Figure 2.6 (a) to (d) shows the overall and intrinsic small signal optical modulation response of the modeled VCSEL at various biasing points at both RT and 85 ˚C. The damping rate, γ, in this context is related to ability of the VCSEL device to convert carriers into photons. If the carrier injection rate is faster than the electron-to-photon conversion rate, excess carrier concentration in the QWs will build up and "choke" the optical modulation response as indicated from the laser resonant frequency effect shown in Figure 2.6. At higher I/I_{TH}, the cavity optical field intensity increases and expedites the stimulated recombination process, and hence the carrier choking effect reduces and resonance peak amplitude decreases. The extracted intrinsic optical modulation response shows a higher -3 dB bandwidth than the overall optical modulation response. This increase of bandwidth can be attributed to the reduction of damping limitation imposed by the electrical parasitic transfer function at high frequency.

By fitting the intrinsic optical bandwidth with the two pole laser transfer function, Eqn. 2.9, the parameters, namely f_R and γ, can be used to estimate both the recombination

lifetime, τ_{rec}, and photon lifetime, τ_p. The -3 dB bandwidth of a VCSEL is proportional to the resonance frequency. Resonance frequency of VCSELs at biasing current higher than I_{TH} is closely approximated as

$$f_R \approx \frac{1}{2\pi}\sqrt{\frac{v_g g' N_p}{\tau_p}} = \frac{1}{2\pi}\sqrt{\frac{v_g g'}{qV_p}\eta_i (I - I_{TH})} = D\sqrt{(I - I_{TH})}, \tag{2.10}$$

where v_g is the group velocity of the photons, g' is the differential gain, N_p is the photon density in the cavity, τ_p is the photon lifetime, V_p is the optical modal volume and η_i is the carrier injection efficiency. The D-factor is related to the slope of resonance frequency, f_R, vs. the diode current, $\sqrt{I - I_{TH}}$. It can be interpreted as the conversion efficiency from electrical input modulation to optical modulation output since higher resonance frequency corresponds to higher modulation bandwidth.

By re-writing Eqn. 2.10 in terms of more fundamental parameters and under the assumption that no spontaneous modes are coupled into stimulated laser emission mode, the relationship between the resonance frequency and the lifetimes, τ_{rec} and τ_p, can be shown more clearly. The re-written Eqn. 2.8 is illustrated as

$$f_R = \frac{1}{2\pi}\sqrt{\frac{v_g g'}{qV_p}\eta_i (I - I_{TH})} = \frac{1}{2\pi}\sqrt{\frac{g' N_{TH}}{g_{TH}} \cdot \frac{1}{\tau_{rec}\tau_p}(I/I_{TH} - 1)}, \tag{2.11}$$

where N_{TH} is the threshold carrier concentration, g' is the material differential gain at laser threshold, and g_{TH} is the material laser threshold gain. As shown in Eqn. 2.11, resonance frequency is inversely proportional to the square root of recombination and photon

lifetimes. This makes physical sense because the lifetimes fundamentally are microwave modulation delays as $f \propto 1/2\pi\tau$. The photon lifetime can be seen as optical signal output delay from the DBR mirror cavity and the recombination lifetime is the fundamental limitation on the input electrical to output optical conversion delay.

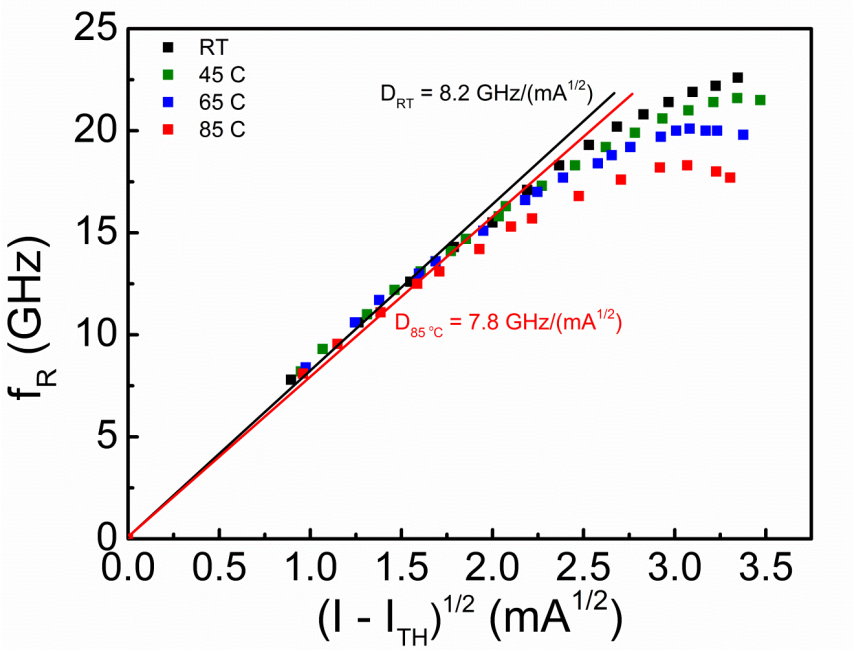

Figure 2.7. Fitted resonance frequency, f_R, vs. $\sqrt{I - I_{TH}}$ graph at RT, 45 °C, 65 °C and 85 °C. The fitted slope of the data points in the linear region corresponds to the D-factor, which is 8.2 GHz/ ($mA^{1/2}$) and 7.8 GHz/ ($mA^{1/2}$) at RT and 85 °C.

By plotting of intrinsic f_R against $\sqrt{I - I_{TH}}$, the D-factor of the VCSEL can be extracted and is shown in Figure 2.7. At high biasing current, the damping rate of the optical response is one of the factors that limit the increase of the resonance frequency and hence the modulation bandwidth. The relationship between γ and f_R can be expressed as,

$$\gamma = Kf_R^2 + \frac{1}{\tau_{rec}} \approx 4\pi^2 \tau_p f_R^2 + \frac{1}{\tau_{rec}}, \tag{2.12}$$

where

$$K = 4\pi\tau_p^2[1 - \Gamma \frac{\partial N}{\partial N_p}] \approx 4\pi\tau_p^2. \tag{2.13}$$

The K-factor, *K*, relates the damping rate, γ, to the resonance frequency, f_R. By plotting the microwave modeling of γ against f_R^2, the photon lifetime, τ_p, and recombination lifetime, $\tau_{rec,}$ can be extracted. Two assumptions were made so the estimated value of τ_p can be extracted from the modeling data. Looking at Eqn. 2.13, the K-factor is also dependent on Γ, the optical confinement factor, and $\partial N / dN_p$. The assumption that the optical modal volume, V_p, is larger than the electrical carrier injection volume, *V*, in the active region is made so the confinement factor, $\Gamma = V / V_p$, is negligible. Furthermore, the assumption that the change of carriers in the active region is comparable to the change of photons is made and therefore, $\partial N / dN_p \simeq 1$. With these two assumptions, the approximation in Eqn. 2.11 is reached.

Figure 2.8 shows that the K-factor, and the photon lifetime, of the VCSEL can be determined from the linear slope and the recombination lifetime can be determined from intercept of the plot γ vs. f_R^2. The extracted recombination and photon lifetimes at RT, 45 ˚C, 65 ˚C and 85 ˚C are summarized in the inset table of Figure 2.8. Both the recombination and photon lifetimes increase as temperature increases from RT to 85 ˚C. The increase of

recombination lifetime is expected. As temperature increases, the carriers on average have higher thermal kT energy and therefore there is a higher chance for carriers to either skip through the quantum wells without being captured or escape out of the quantum well after being captured [30, 31]. These physical phenomena will, hence, result in higher recombination lifetime.

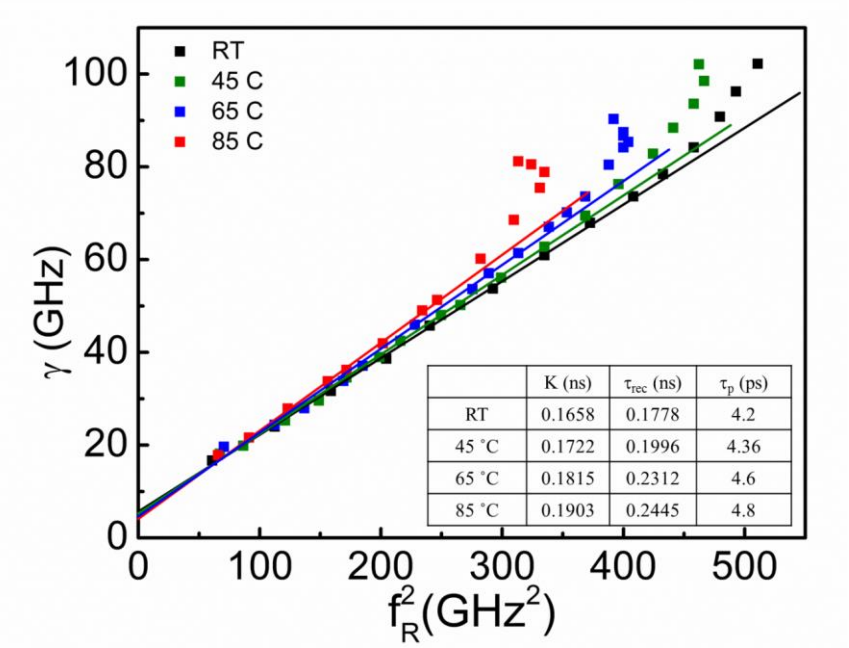

	K (ns)	τ_{rec} (ns)	τ_p (ps)
RT	0.1658	0.1778	4.2
45 °C	0.1722	0.1996	4.36
65 °C	0.1815	0.2312	4.6
85 °C	0.1903	0.2445	4.8

Figure 2.8. Fitted damping rate, γ, vs. fitted resonance frequency squared, f_R^2, at RT, 45 °C, 65 °C and 85 °C. The extracted K-factor, recombination lifetime, τ_{rec}, and photon lifetime, τ_p are listed in the inset table.

On the other hand, the increase of photon lifetime is likely associated with the change of refractive index in the high/low alternating index $Al_xGa_{1-x}As$ p-DBR mirror stack. The refractive index in semiconductor materials can be altered by carrier-induced change. From experimental data and theoretical calculation, the refractive index of semiconductor decreases as the carrier concentration increases [32, 33]. For a p-DBR stack

with more than 20 pairs of high/low Al content $Al_xGa_{1-x}As$ layers ($Al_{0.9}Ga_{0.1}As/Al_{0.12}Ga_{0.88}As$), there are more deep trap levels in the high Al content layers ($Al_{0.9}Ga_{0.1}As$) and, on top of it, there are interface trap levels between the high/low Al content transition thin layers. As temperature increases, the hole carriers in the deep trap levels may gain enough thermal energy to escape the trap levels and become free carriers adding to the hole carrier concentration. This is reflected on the increase of conductivity and, therefore, the reduction of differential resistance at higher temperature.

The photon lifetime is related to photon loss rate out of the optical cavity; longer photon lifetime at higher temperature indicates less photon loss. The less photon loss rate can be attributed to the reduction of material absorption (α_i) and the decrease of the mirror loss (α_m). In this case, the decrease of the mirror loss is related to the increase of the contrast of refractive index of the p-DBR stack. The decrease of refractive index in high Al content of $Al_{0.9}Ga_{0.1}As$ layers at higher temperature can be attributed to more thermally induced carriers from the deep and interface trap levels contributing to a higher hole concentration. Therefore, the contrast of refractive index between the high/low content $Al_xGa_{1-x}As$ layers increases.

The effect of thermally induced increase of carrier concentration in the low Al content can be neglected as deep level concentration is insignificant for Al content below 0.3 [34]. Therefore, it can be assumed that only the refractive index of the high Al content decreases and this leads to a larger contrast of refractive indexes between the alternating Al content p-DBR mirror layers. Resulting from the further refractive index contrast, the

optical cavity provides a better photon confinement, Q factor, and hence the average time that takes a photon to leave the p-DBR mirror stack, τ_p, increases.

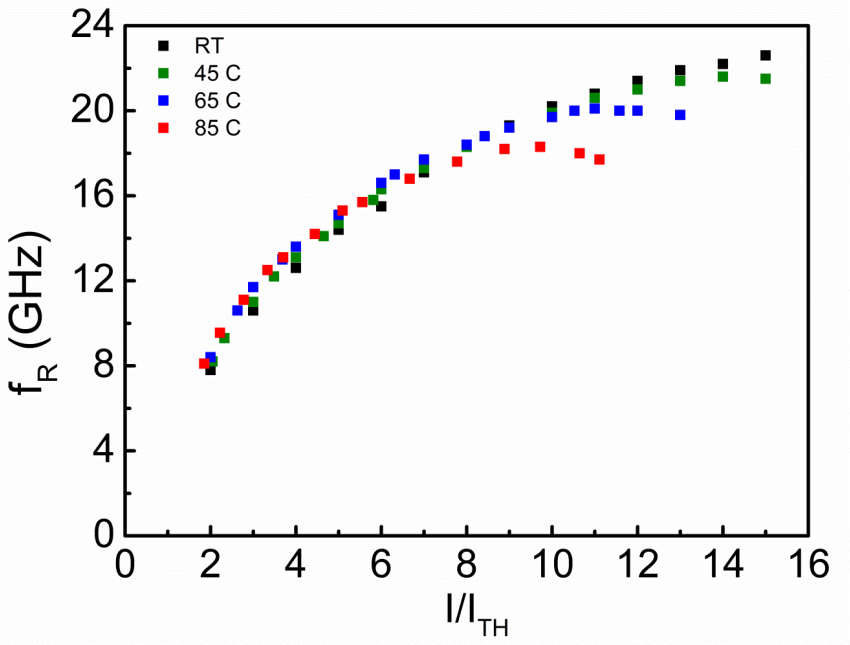

Figure 2.9. Fitted resonance frequency, f_R, vs. I/I_{TH} at RT, 45 °C, 65 °C and 85 °C. Notice the difference between each temperature becomes more obvious when $I/I_{TH} > 7$.

To gain more insights into the fitted parameters such as τ_{rec}, and τ_p, a comparison between f_R for different temperatures at approximately the same I/I_{TH} can be made. According to Eqn. 2.11, f_R is proportional $\sqrt{(I/I_{TH}-1)}$ and inversely proportional to $\sqrt{\tau_{rec}\tau_p}$. Therefore, at the same I/I_{TH}, f_R should be lower for higher temperature as both recombination and photon lifetimes are longer at higher temperature. Figure 2.9 shows f_R against I/I_{TH} at RT, 45 ˚C, 65 ˚C and 85 ˚C. At $I/I_{TH} \leq 7$, f_R at the four different temperatures are close to each other; within 10% of highest value. The similarity in value

can be attributed to temperature-dependent material parameters, such as differential gain and threshold carrier concentration, and f_R fitting uncertainty errors. After $I/I_{TH} > 7$, the f_R difference between each temperature becomes more pronounced. The increasing difference can be attributed to the larger and earlier, with respect to I/I_{TH}, thermal roll off limitation of f_R. From f_R fitted value and extracted τ_{rec} and τ_p, the product of $\sqrt{g' N_{TH}/g_{TH}}$ can be further extracted as shown in Eqn. 2.8. Calculated differential gain, g', threshold carrier concentration, N_{TH}, and threshold gain, g_{TH} of an active region that is similar to the discussed VCSEL structure can be found in [35]. The extracted product of material parameters is 1.21 at RT. Compared to the calculated value, 1.43, the two values are in good agreement.

2.3 High-Speed Data Transmission Performance

To test the data transmission capability of the VCSEL, the large signal transmission eye diagrams and bit-error rate (BER) were measured. The large signal transmission test is performed on the VCSEL using an SHF 57 Gb/s pattern generator with non-return-to-zero 2^7-1 pseudorandom binary sequence (PRBS7) with a peak-to-peak voltage swing of V_{pp} = 0.65 V. The electrical data signal from the patterned generator is combined with the DC bias through an SHF 67 GHz bias Tee, and the coupled optical output is relayed into a New Focus 22 GHz high-gain photodetector with a 3 m back-to-back (BRB) OM4 optical fiber. To measure the eye diagrams, the converted electrical signal from the photodetector

is sent to an Agilent sampling oscilloscope with 70 GHz bandwidth module. On the other hand, to measure the BER, the converted electrical signal is sent to an SHF 60 Gb/s error analyzer.

The eye diagrams can be used to analyze the signal integrity of the data transmission. Qualities such as rise/fall time, jitter, optical modulation amplitude etc. can be statistically extracted from the eye diagrams. The eye diagrams for the VCSEL under the biasing conditions of I = 12 mA & 57 Gb/s V_{pp} = 0.65 V at RT and I = 10 mA & 50 Gb/s V_{pp} = 0.65 V at 85℃ data transmission are shown in Figure 2.10. In order to achieve as few errors as possible, optimization of the eye diagrams integrity through tuning the electrical injection signals and optical coupling is essential.

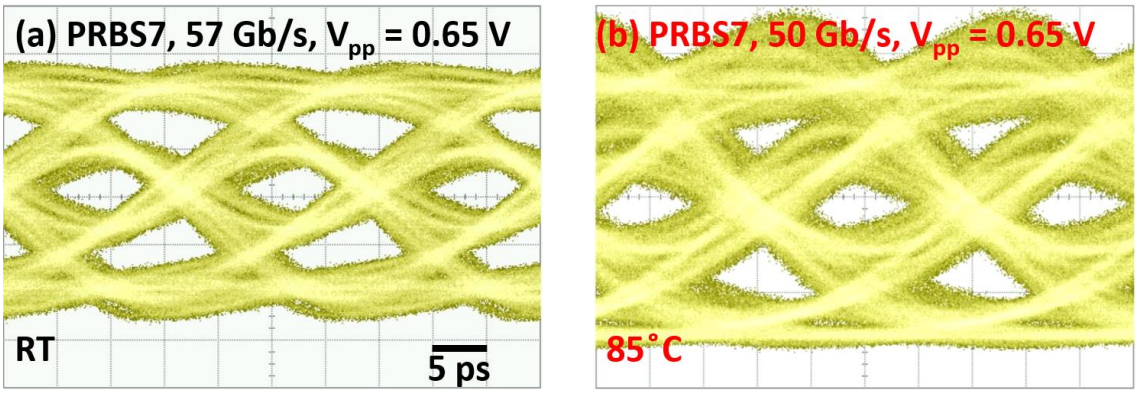

Figure 2.10. Large signal modulation data transmission eye diagrams for the 5 μm optical aperture VCSEL under the biasing conditions of (a) I = 12 mA & 57 Gb/s V_{pp} = 0.65 V at RT and (b) I = 10 mA & 50 Gb/s V_{pp} = 0.65 V at 85℃.

To ultimately analyze the signal transmission performance of the VCSEL, the BER test is performed. To be able to relate BER to received optical power, a variable neutral density filter is used to attenuate the optical power coupled into the BTB optical fiber.

Figure 2.11 shows the BER vs. received optical power plot for the corresponding eye diagrams shown in Figure 2.10. In datacom industry standard, an error-free transmission is defined as being able to reach BER < 10^{-12}. Furthermore, to ensure > 99% statistical confidence level, ≥ 10 Tb, 10^{13} bits, of data was collected for each point shown in Figure 2.10. From Figure 2.10, it can be seen that the VCSEL is capable of achieving error-free transmission for 57 Gb/s at RT and 50 Gb/s at 85℃ with received optical power greater than 2 mW (3 dBm).

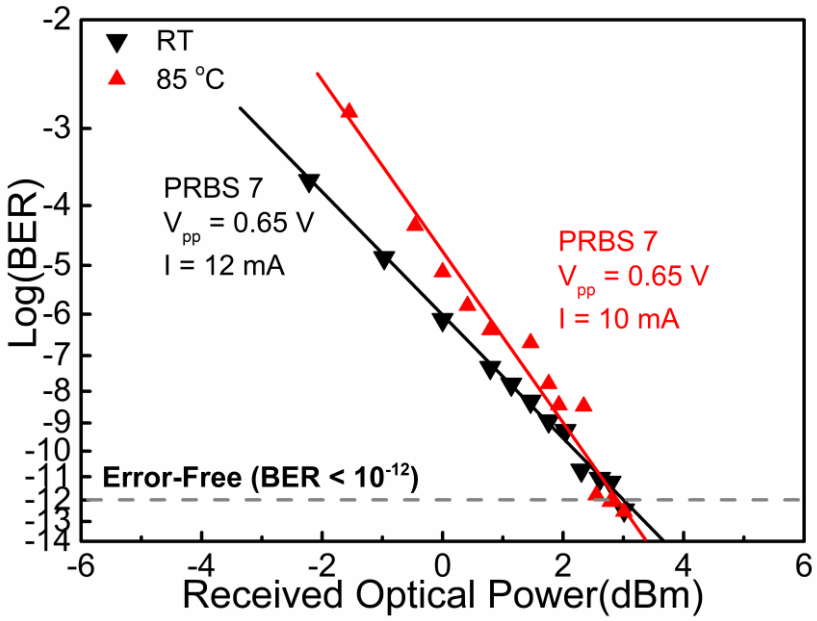

Figure 2.11. BER versus received optical power measured for 5 μm optical aperture VCSEL at RT and 85℃. The highest error-free transmission rates are 57 Gb/s and 50 Gb/s at RT and 85℃ accordingly. Error-free transmission could be achieved when the received optical power is ≥ 2 mW (3 dBm) as observed from the graph.

At the bias I = 12 mA at RT and I = 10 mA at 85℃, the VCSEL's differential resistance is around 53 and 58 Ω, derived from the I-V characteristics. Due to the better impedance match to standard 50 Ω of testing instruments, no external amplification was

implemented to achieve the error-free transmission results. Higher-speed error-transmission could possibly achieved with amplification on V_{pp} to obtain better OMA. With the electrical power consumption of the VCSEL, $P_{Electrical} = I \times V$, the energy per bit efficiencies for the data transmission of 57 Gb/s at RT and 50 Gb/s at 85℃ are calculated to be 536 and 456 fJ/bit accordingly.

2.4 Transition from VCSEL to VCTL

As shown in the microwave analysis, the state-of-the-art high-speed VCSEL has a spontaneous recombination lifetime, τ_{rec}, limited to nanosecond range and it is projected that the bandwidth of the VCSEL will be limited to ~30 GHz. Figure 2.12 shows the simulation results that illustrates the effect of spontaneous recombination lifetime on bandwidth.

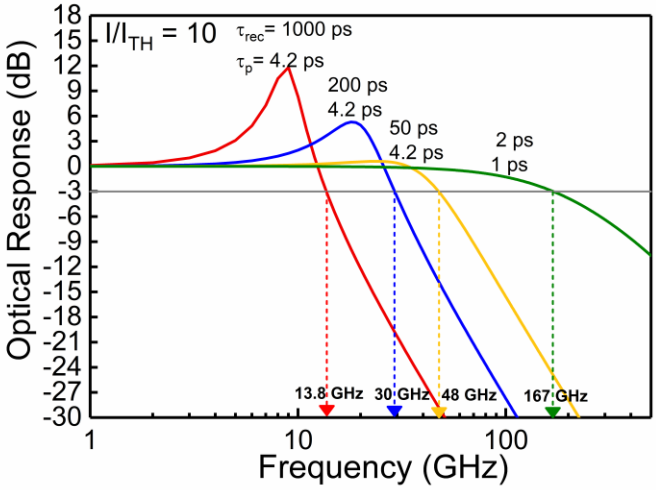

Figure 2.12. Simulated optical frequency response at I/I_{TH} = 10 and various τ_{rec} and τ_p combinations. As τ_{rec} decreases, the theoretical -3 dB bandwidth increases and the resonance amplitude decreases. Physically, this corresponds the laser device capable of alleviating carriers chocking effect in the QW.

The microwave analysis shows VCSELs are limited by a τ_{rec} of 200 ps and it corresponds to an intrinsic bandwidth of 30 GHz with a high Q cavity confining the photon lifetime, τ_p, of 4.2 ps. Theoretically, if τ_{rec} is reduced down to 50 ps or even 2 ps and τ_p is adjusted to avoid over-damping of the system, the -3 dB bandwidth can be extended to 48 GHz and 167 GHz. On top of it, the resonance amplitude is greatly reduced due to higher damping for the reduction of τ_{rec}. Physically, this corresponds to the laser device having better capability to alleviate the carrier choking effect in the QW. The reduction of resonance amplitude is also favorable for data transmission. Fundamentally, a resonance in the frequency domain corresponds to oscillation in the time domain. Oscillation could severely degrade the signal integrity of the transmission as shown in a simulated 100 Gb/s data transmission in Figure 2.13 (a) and (b).

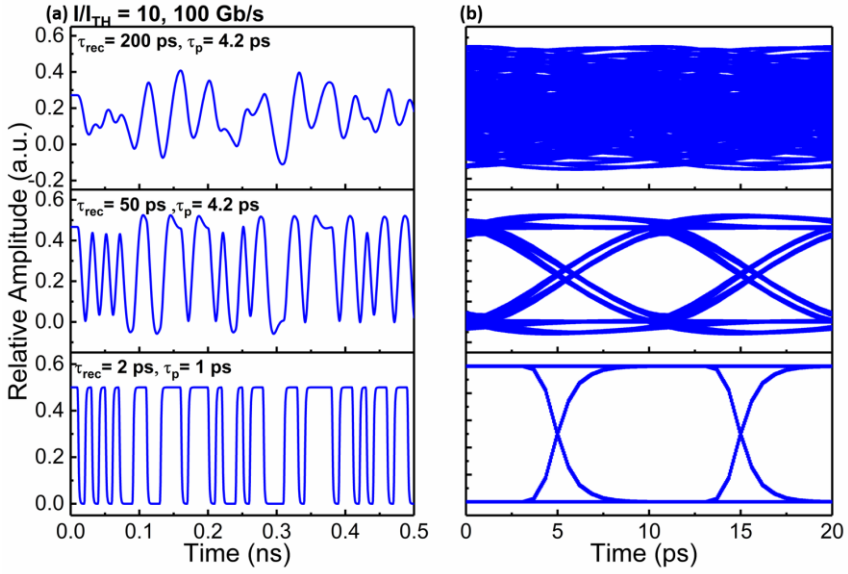

Figure 2.13. Simulated 100 Gb/s data transmission at I/I_{TH} = 10 for the τ_{rec} and τ_p combinations shown in Figure 2.12: (a) The waveform pattern and (b) the eye diagram of the data transmission. As τ_{rec} decreases down to 2 ps, waveform pattern shows less oscillation and the eye diagrams exhibit much higher signal-to-noise ratio.

In order to break the bandwidth bottleneck, fundamentally the recombination lifetime needs to be reduced. The limitation of recombination lifetime in a p-i-n DL structure is carrier dynamics. In Figure 2.14 (a), a schematic energy band diagram illustrates the carrier dynamics in a p-i-n DL. The carriers accumulate in the quantum wells and wait to recombine and thus result in a slow recombination lifetime. The nanosecond recombination lifetime not only limits the modulation bandwidth but also leads to a large resonance peak in the frequency response due to the relaxation oscillation at low bias current. The resonance peak can potentially cause inter-symbol interference and degrade the signal integrity.

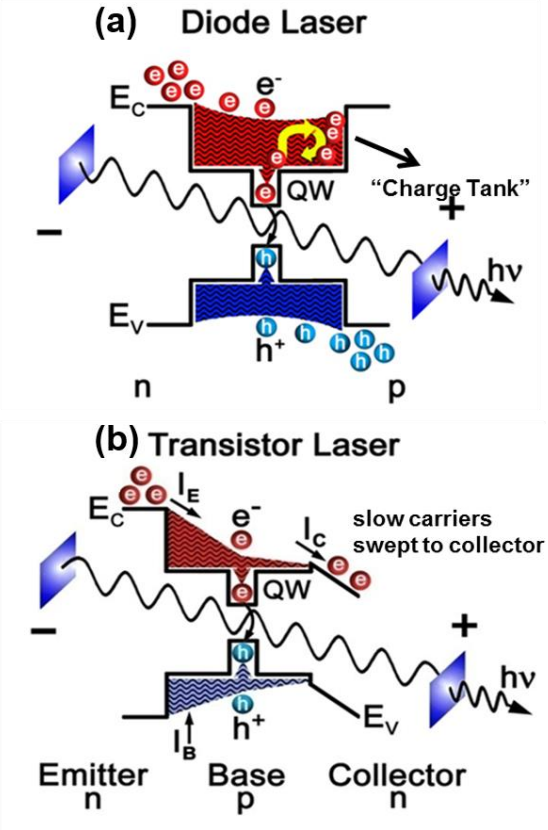

Figure 2.14. Schematics energy band diagram and electrical carrier distribution in an (a) p-i-n diode laser and (b) n-p-n hetero-junction bipolar transistor laser.

On the other hand, in TL operation, hole and electron transport in the base are established by fast processes governed by dielectric relaxation time and submicron base diffusion transit time, shown to be ~2 ps, due to the tilted charge profile in the base-collector junction [16, 36]. Slow carriers that do not recombine in time are forced by the potential difference at the base-collector junction to the collector contact instead of "waiting" to recombine. The tilted charge profile is illustrated in Figure 2.14 (b). The reduced recombination lifetime not only improves the optical modulation but also lowers the resonance bump. Edge-emitting transistors have exhibited resonance-free optical frequency response over 20 GHz modulation bandwidth [37], simultaneous electrical and optical "open-eye" signals operated at 40 Gb/s data rate [38], and achieved error-free data transmission at 22Gb/s [39]. By further scaling with a high-Q vertical cavity, the VCTLs are expected to have compact geometry, low threshold, and high modulation bandwidth in addition to the edge-emitting TL characteristics. Thus, VCTLs are promising devices for 100 Gb/s transceivers for short-reach optical interconnects.

2.5 Summary

In this chapter, we have developed a microwave extraction method to accurately determine radiative recombination lifetime and an equivalent circuit modeling technique used to de-embed the electrical parasitic transfer function and obtain the intrinsic optical response for diode lasers or VCSELs. For a state-of-the-art high-speed 5 μm aperture oxide-confined VCSEL, The extracted intrinsic modulation bandwidth is 31.86 GHz and 26.19 GHz at RT and 85 °C. With the same technique, we have also illustrated a method

to empirically extract the recombination and photon lifetimes of VCSEL. The extracted τ_{rec} and τ_p are 0.1778 ns and 4.2 ps at RT and 0.2445 ns and 4.8 ps at 85 °C. Similar technique can be applied to TL with a more complex equivalent circuit model to include the transistor three terminal structure [40]. The fundamental bandwidth limitation of VCSEL is illustrated through carrier dynamics and subsequently VCTL is presented to be a promising candidate to break the bandwidth bottleneck.

3. DEVELOPMENT OF HIGH-SPEED OXIDE-CONFINED VERTICAL CAVITY TRANSISTOR LASER (VCTL)

The first VCTL was demonstrated in 2012 by incorporating a light emitting transistor (LET) into a DBR mirror stack; however, due to lack of confinement, the device showed a large threshold (> 3 mA), and low optical output (< 5 μW). By developing a selective oxidation process, the stimulated recombination has been greatly enhanced; hence, the laser threshold is reduced to 1 mA and the coherent laser output is amplified to 500 μW. With the shallow oxidation to seal off the sidewall first, and a trench defined by ICP etching as an opening for selective lateral oxidation to cut off undesired current path that results in non-radiative recombination, a better confined cavity is achieved to support coherent stimulated emission recombination. Most of the unwanted recombination results from the current underneath the emitter metal. Nevertheless, a large emitter resistance still exists from the long top DBR current path. An emitter resistance of 603 Ω is estimated from the V_{CE} offset on the $I_C - V_{CE}$ family curves. The large resistance limits the bandwidth of the device as the injected signal is attenuated severely before reaching the active region. Nevertheless, a bandwidth of 11.1 GHz was observed for a oxide-confined VCTL with an optical aperture of 4.7 × 5.4 μm^2. To improve the bandwidth performance, the emitter resistance needs to be reduced. A direct way to do so is to partially etched down the top DBR mirror and place the emitter contact closer to the active region. The partially etched VCTL is fabricated and characterized through DC and RF analysis. Although emitter resistance is greatly reduced, large laser current threshold and large parasitic inductances are observed for the partially etched VCTL. The origins of the newly discovered problems

are attributed to the formation of low Q sub-cavity from the incomplete selective lateral oxidation.

3.1 Design of Oxide-Confined VCTL

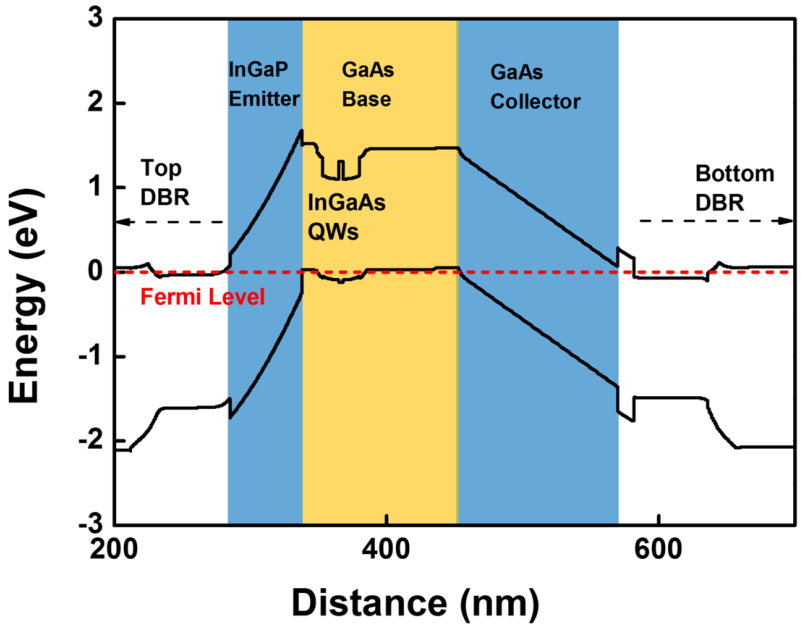

Figure 3.1. Energy band diagram of the HBT/LET structure in the n-p-n VCTL.

Similar to a VCSEL's material structure, a VCTL's material structure includes top and bottom DBR mirrors with an n-p-n light emitting transistor (LET) structure sandwiched between them. From bottom to top, the 980 nm VCTL starts with 36 pairs of n-doped $Al_{0.12}Ga_{0.88}As/Al_{0.9}Ga_{0.1}As$ DBR, followed by a highly n-doped sub-collector GaAs layer. Then the LET structure is grown in the 1-λ cavity. Between the sub-collector and the collector, there is a thin $In_{0.49}Ga_{0.51}P$ etching stop layer. The collector is a 116 nm lightly n-doped GaAs. The 116 nm base is composed of heavily p-doped GaAs layers

followed by the intrinsic MQW region with two 12 nm $In_{0.12}Ga_{0.88}As$ with GaAs barriers and an $Al_{0.05}Ga_{0.95}As$ layer for better carrier confinement. The emitter is an n-doped wide-gap 53 nm $In_{0.49}Ga_{0.51}P$ layer. Above the LET structure is the top n-DBR stack made of 1 pair of $Al_{0.12}Ga_{0.88}As/Al_{0.98}Ga_{0.02}As$ and 24 pairs of $Al_{0.12}Ga_{0.88}As/Al_{0.9}Ga_{0.1}As$. The $Al_{0.98}Ga_{0.02}As$ is to be laterally oxidized for confinement. Figure 3.1 shows the energy band diagram of the VCTL layer structure. Due to the heavy p-type doping, the Fermi level is lower than the valence band edge of the base. Compared with an edge-emitting TL, the VCTL design has specific characteristics for a surface-emitting laser. First, quantum wells in the VCTL are placed near the emitter to match the antinodes of the photon field. Second, the total thickness of emitter-base-collector needs to match the 980 nm emission cavity, $L = \lambda / n_c$. Instead of modifying the base, we fix the base thickness while increase the collector thickness. The device's collector transit time may increase but result in lower base-collector capacitance and higher breakdown voltage. As shown in the previous work, the VCTL can operate at $V_{CE} > 6V$, which gives higher operational range [41].

The fabrication of the oxide-confined VCTL starts with SiN_x deposition by PECVD then patterned by photolithography and RIE to form a hard mask for the top DBR mesa ICP etching. The DBR mesa is created by ICP etching with BCl_3 plasma and the etching is stopped on the $In_{0.49}Ga_{0.51}P$ emitter. The sample is then transferred to a wet oxidation furnace for a shallow oxidation, sealing of DBR sidewalls, at 425 °C. Then, the SiN_x is removed, and a second SiN_x is deposited to protect the sidewall of the DBR mesa and simultaneously serve as mask for the second ICP etching. The second ICP etching opens a trench on the DBR mesa for a long lateral oxidation process.

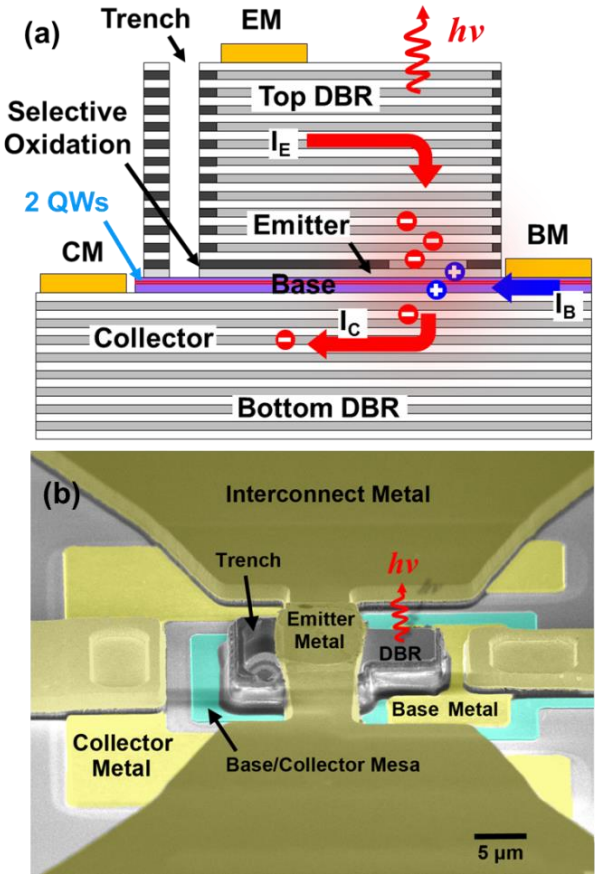

Figure 3.2. (a) The schematic device diagram of a vertical cavity transistor laser (VCTL). The lateral oxidized layer underneath the emitter metal for current and optical confinement is achieved by trench opening and deep oxidation. (b) False colored scanning electron microscopic image of the VCTL.

The trench oxidation is used to eliminate the undesired recombination underneath the emitter metal, as described previously, and form the optical aperture at the emission area part of the mesa. The SiN_x is then removed by RIE, and the $In_{0.49}Ga_{0.51}P$ emitter is removed by HCl to expose the base. The base/collector mesa is defined by photolithography and citric acid wet etching. Because of the selectivity, the wet etching stops on the $In_{0.49}Ga_{0.51}P$ etching stop layer. The $In_{0.49}Ga_{0.51}P$ etching stop is removed by HCl to expose the sub-collector for collector contact. Ti/Pt/Au p-type base contact metal is evaporated onto the base/collector mesa, and then AuGe/Ni/Au n-type contact metal is evaporated onto the

DBR mesa and the sub-collector layer. The n-type contact is annealed at 310 °C for 10 min to form ohmic contacts. Polyimide is then coated and cured at 270 °C for passivation. The via-holes are then defined by photolithography and opened by RIE with O_2. Finally, Ti/Au interconnect metal is evaporated. Figure 3.2 shows the (a) cross-sectional schematic and (b) false colored SEM image of the VCTL. Due to the mismatch between the QW emission wavelength and the cavity length design, the VCTL can only exhibit laser operation at low temperature.

The common-emitter collector output (I_C-V_{CE}) characteristics and the corresponding optical output characteristics (L-V_{CE}) for a VCTL with a 5.4 × 4.7 μm^2 aperture are shown in Figure 3.3 (a) and (b) with V_{CE} swept from 0 to 6 V, with I_B increasing 0.2 to 6 mA in ΔI_B = 0.2 mA at T = 80 K. In the $I_C - V_{CE}$ family characteristics, the large I_B dependent V_{CE} offset at I_C = 0 mA is attributed to the high emitter series resistance from the top DBR mirror which leads to an up unbalanced voltage drop across the device, $V_{CE} = V_{CB} + V_{BE}$. By solving V_{CE} from the Ebers-Moll circuit model with I_C = 0 mA, V_{CE} offset is expressed as,

$$V_{CE,offset} = R_E I_B + \frac{kT}{q}\ln\left(\frac{A_C J_{CS}}{\alpha_N A_E J_{ES}}\right) - A_C J_{CS}\left[e^{\frac{qV_{BC}}{kT}} - 1\right], \tag{3.1}$$

where α_N is the forward current gain, and J_{ES} and J_{CS} are the emitter and collector saturation current density at $V_{BC} = V_{CE} = 0$, respectively. A_E and A_C are the dimensions of emitter and collector. From Eqn. 3.1, the V_{CE} offset is proportional to I_B by the emitter resistance, R_E. By approximating the first term of Eqn. 3.1 to be the most dominant term, the emitter resistance ca be estimated as

$$R_E \approx \frac{\Delta V_{CE,offset}}{\Delta I_B}. \tag{3.2}$$

Through this analysis, the emitter resistance is determined to be 603 Ω. At low I_B bias, the collector I_C-V_{CE} curves shown in black indicate the VCTL operates in the spontaneous emission region, while the total emission power in the L-V_{CE} curves is below 15 μW.

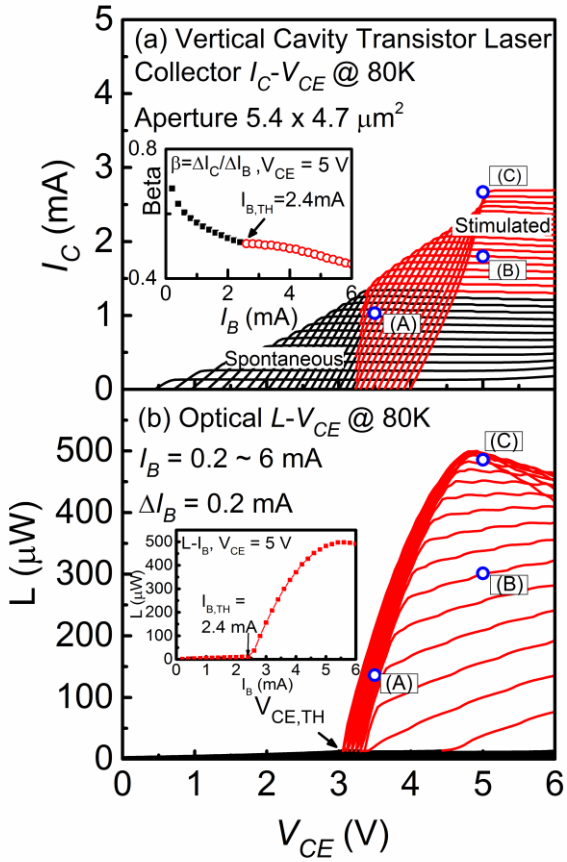

Figure 3.3. (a) I_C-V_{CE} and (b) optical L-V_{CE} output family characteristics at 80 K of a 4.7 × 5.4 μm^2 VCTL. The base-current threshold, $I_{B,TH}$ = 2.4 mA (V_{CE} = 5 V), and collector-voltage threshold, $V_{CE,TH}$ = 3.2 V (I_B = 6 mA), indicate the transition from spontaneous (black) to stimulated emission (red). The gain compression of VCTL in the I_C-V_{CE} family curves inset exhibits the base shifting recombination operation from spontaneous to stimulate with increasing base current and the L-V_{CE} confirms that $I_{B,TH}$ = 2.4 mA at V_{CE} = 5 V. The maximum VCTL output power is ~ 0.475 mW.

When $I_B > I_{B,TH}$ = 2.4 mA above the laser threshold current, $I_{B,TH}$, the VCTL switches to stimulated emission, and the emission intensity exhibits a large jump (red curves) from 15 μW to 475 μW. The inset of L-V_{CE} family curves confirms that $I_{B,TH}$ = 2.4 mA at V_{CE} = 5 V. The inset of I_C-V_{CE} family curves shows the I_B dependent current gain ($\beta = \Delta I_C/\Delta I_B$) at V_{CE} = 5 V. The unique current gain (β) compression phenomenon of a transistor laser decreases from 0.67 to 0.44 also indicating the base shifting operation from spontaneous to stimulated recombination [15]. From the L-V_{CE} characteristics, the collector voltage threshold ($V_{CE,TH}$) is observed for stimulated emission. As V_{CE} increases above $V_{CE,TH}$, the base recombination is then sufficient to sustain the laser operation, while the base hole leakage to the collector is greatly reduced as the base-collector junction hole barrier is larger due to more reversed-biasing. One interpretation of the large $V_{CE,TH}$ is due to unbalanced voltage drop across the device. For a common-emitter HBT to be in forward active mode, both junctions, emitter-base (EB) and base-collector (BC), need sufficient voltage applied. In our case the EB forward biased junction turns on faster than the BC reversed biased junction due to large emitter resistance.

Figure 3.4 shows the optical spectra of the VCTL at I_B = 2, 3, 4 mA and V_{CE} = 5 V. At I_B = 2 mA, the magnified spectrum exhibits spontaneous emission with three distinct cavity modes near 968 nm. When $I_B > I_{B,TH}$, the fundamental cavity mode becomes dominant. At I_B = 4 mA, the stimulated recombination exhibits a peak at 970.96 nm with a full wave at half maximum (FWHM) of 0.23 Å corresponding to a cavity quality factor, Q, of 42,216 ($Q \approx \nu/\Delta\nu$). The inset shows the corresponding optical spectrum, log scale, with the VCTL exhibits quasi-single-mode operation and side-mode suppression ratio (SMSR) of

31.76 dB. The measured mode-spacing between fundamental and first-order modes are 1.09 nm and 1.42 nm. For a rectangular aperture, the dimensions can be accurately determined to be 5.4 × 4.7 μm^2 from the measured mode-spacing from solving the Helmholtz equation.

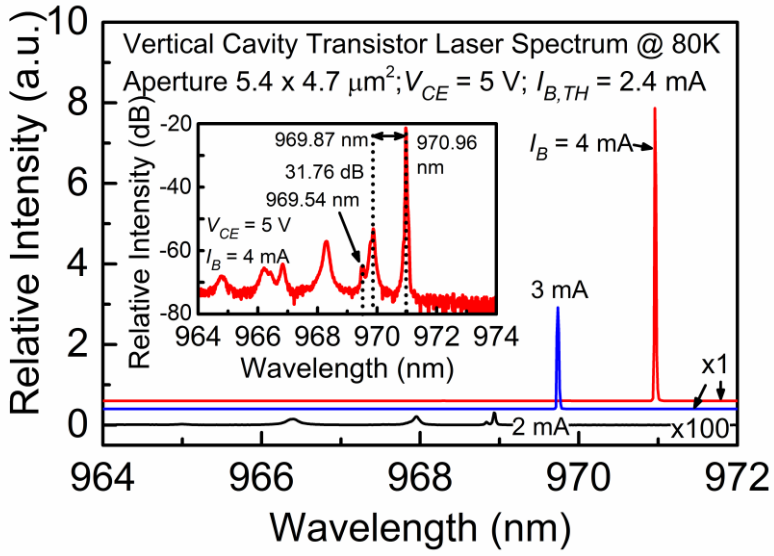

Figure 3.4. Emission spectra of a 5.4 × 4.7 μm^2 VCTL at I_B = 2, 3, and 4 mA. When I_B = 2 mA, the magnified spontaneous spectrum exhibits three distinct peaks near 968 nm. When $I_B > I_{B,TH}$, the fundamental mode dominates. The inset shows spectrum in log scale lasing peak at 970.96 nm with a side-mode suppression ratio (SMSR) of 31.76 dB.

Figure 3.5 shows the measured modulation characteristics at 80 K of the common-emitter VCTL at three different biases. At biasing condition A, V_{CE} = 3.5 V and I_B = 3.6 mA, the device is operated in the saturation mode with base-emitter (BE) and base-collector (BC) in forward bias. In this mode of operation, the carriers injected from the junctions piles up in the active region (similar to diode laser) and the stored charge delays in recombining in the quantum wells, resulting in a a lower f_{-3dB} = 6 GHz. When the device is biased at condition B, V_{CE} = 5 V and I_B = 3.6 mA, the BC junction becomes reversed-

biased and the device operates in the forward active mode. In the forward active mode, the carrier lifetime is pinned to the fast transit time. Thus, a higher bandwidth f_{-3dB} = 9 GHz is obtained. Further increase of the cavity photon density with I_B = 6 mA, biasing condition C, enhances f_{-3dB} to 11.1 GHz.

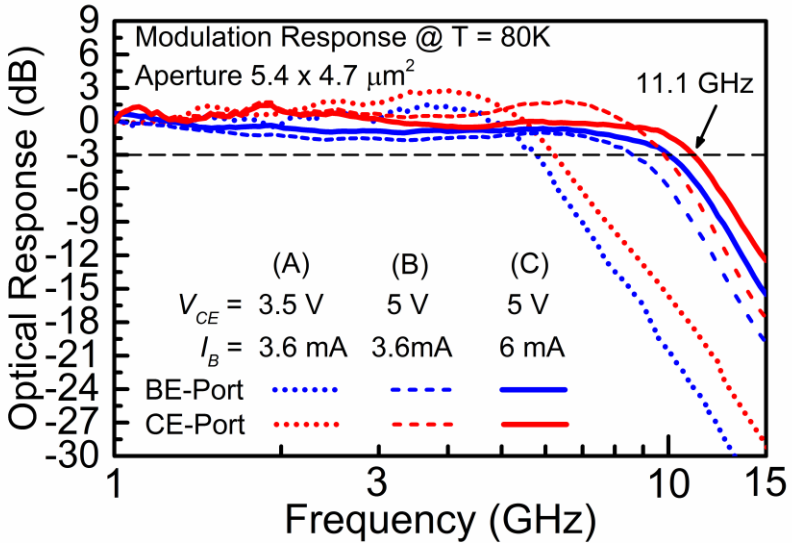

Figure 3.5. Resonance-free optical responses of the modulated common-emitter VCTL are measured with BE input (blue) or CE input (red) at three different biases. A maximum f_{-3dB} = 11.1 GHz resonance-free optical response is observed.

The device optical frequency response for both base current or collector voltage modulation exhibits very low laser-resonance peak up to 11 GHz despite the high emitter resistance of 603 Ω. This is a result of the intrinsically fast carrier lifetime for VCTL. In addition to the conventional current modulation (δI_B) at the BE port, the VCTL can also be directly voltage modulated (δV_{CE}) at the CE port. Essentially, the voltage modulation on the CE port is affecting the intra-cavity photon-assisted tunneling (ICpaT) process and the physics of ICpaT will be illustrated in detail in Chapter 4. From Figure 3.5, it can be seen that the bandwidth is consistently higher when the modulation is applied on the CE port.

This suggests that ICpaT modulation is a faster and more efficient way of modulating VCTLs than the current injection modulation. With further reduction of parasitics and more refined design and scaling, we expect the VCTL will be an excellent low power laser for high-speed and high-signal integrity data communication.

3.2 Reduction of Parasitic Resistance for High-Speed Performance

The excessive emitter series resistance has caused the VCTL to exhibit large voltage offset in the I_C-V_{CE} family curve and require a higher V_{CE} bias to operate in the forward-active mode. In a VCTL, the stimulated emission is determined by the holes supplied into the base via I_B, the electron injection from the emitter to the base via the forward-biased emitter/base junction (V_{BE}), and the reverse bias on the base/collector junction (V_{BC}) which determines the boundary condition at the base/collector junction. In our VCTL measurement, the device is biased in common-emitter configuration with I_B and V_{CE} bias. V_{CE} is the sum of V_{CB} and V_{BE}, so a higher emitter series resistance leads to a higher V_{CE} bias required for the intrinsic HBT to have sufficient bias across the junctions.

To reduce the emitter series resistance, we have developed a new fabrication process to partially etched the top DBR mesa and place the emitter contact closer to the base/active region. In order to achieve the partial etch, a new layer of SiN_x mask needs to be implemented. Figure 3.6 shows the cross-sectional schematics and the corresponding SEM top view image of the steps used to manifest the partially etched structure. First a SiN_x mask is defined for the "emission area" of the mesa ICP etch. Instead of stopping at the $In_{0.49}Ga_{0.51}P$ emitter, the etch stopped at an $Al_{0.12}Ga_{0.88}As$ layer 2.5 pairs of $Al_{0.9}Ga_{0.1}As$/ $Al_{0.12}Ga_{0.88}As$ DBR mirror stacks above the $Al_{0.98}Ga_{0.02}As$ oxidizing layer.

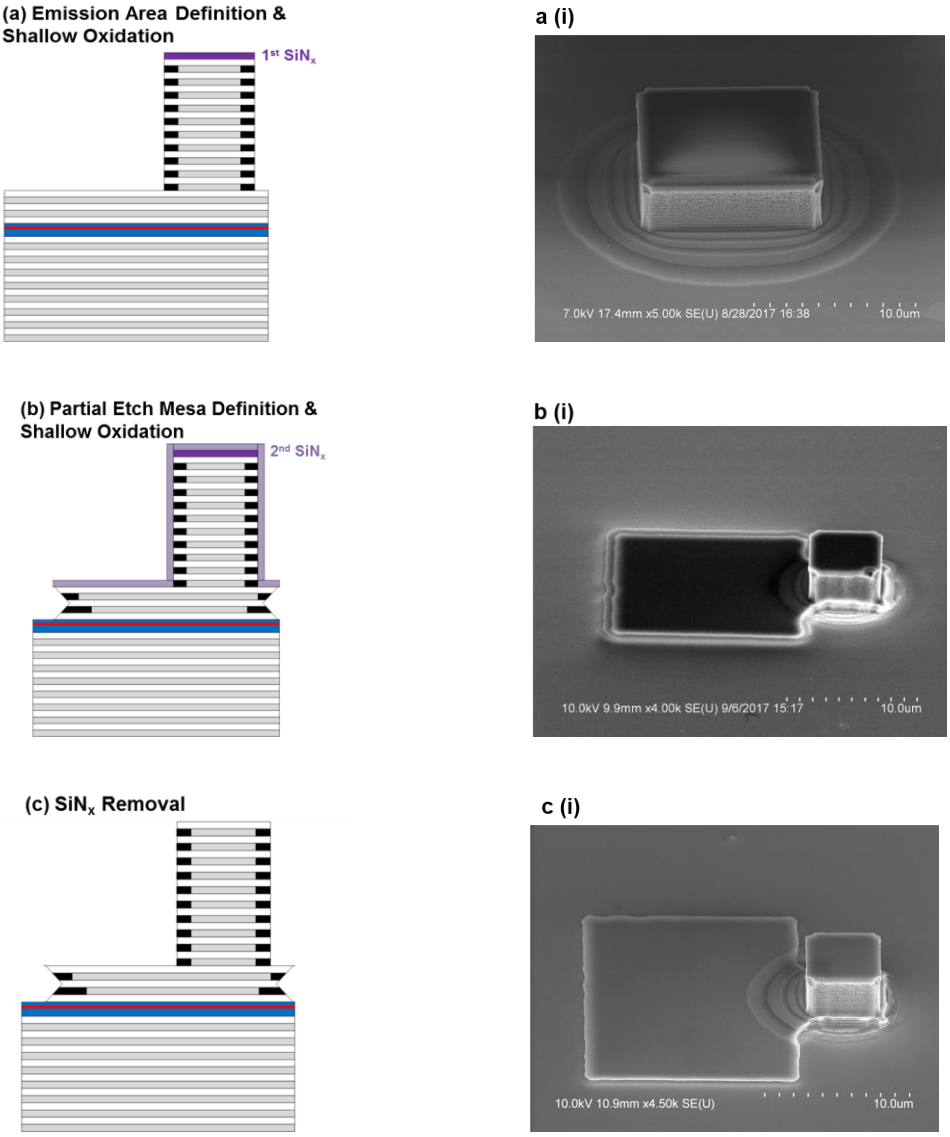

Figure 3.6. The schematics and SEM image of each fabrication steps developed to complete the partial etch process. (a) First SiNx mesa is defined for the emission area. After the ICP etch is executed, a shallow oxidation is performed to seal of the DBR sidewalls. (b) Second SiN_x mask is defined for the top DBR mesa and the mesa is created with H_2SO_4 based wet etch. Another shallow oxidation is ensued to seal of the newly etched sidewalls. (c) Last, by removing the SiN_x mask, the partially etched top DBR structure is manifested.

A shallow oxidation is ensued to seal off the sidewall. Second, another SiN_x mask is defined to outline the top DBR mesa, encompassing the emission area with an 0.5 µm offset. The top DBR mesa is created with H_2SO_4 based wet etch solution. Last, by removing

the SiN_x mask, the partially etched structure is manifested and the rest of the pre-established VCTL fabrication follows. The extra 0.5 µm mesa around the emission area might potentially increase the extrinsic base resistance as the longer current path corresponds to larger sheet resistance. Nevertheless, this mesa can act as a sacrificial layer for etch foot removal wet etch. It is a common phenomenon that ICP dry etching results in an unwanted etch foot near the base of the etched structure and the length of the etch is roughly 1:1 to the etching depth. Therefore, for an etch in the µm range, it is critical to remove the etch foot to place the base contact on the correct layer.

3.3 Characteristics of Partially Etched VCTL

The developed partially etching processing technique has been implemented into fabricating devices hence yielding the first partially etched VCTL. The finished device false colored SEM image, without planarization and metal interconnect, is shown in Figure 3.7.

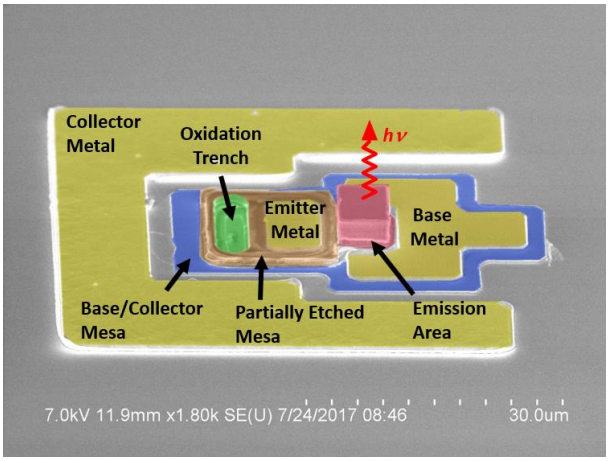

Figure 3.7. False colored SEM image of the partially etched VCTL. The partially etching processing technique is implemented into fabricating the first partially etched VCTL. As a result, the emitter metal is placed closer to the base QW active region.

We identified that the top DBR emitter resistance, estimated to be 603 Ω, is the most severe parasitic that limits the intrinsic bandwidth performance of VCTL as it contributes to a large *RC* time delay constant. In order to realize the intrinsic performance of the VCTL, reducing the emitter resistance is a straightforward approach without redesigning the epitaxial structure.

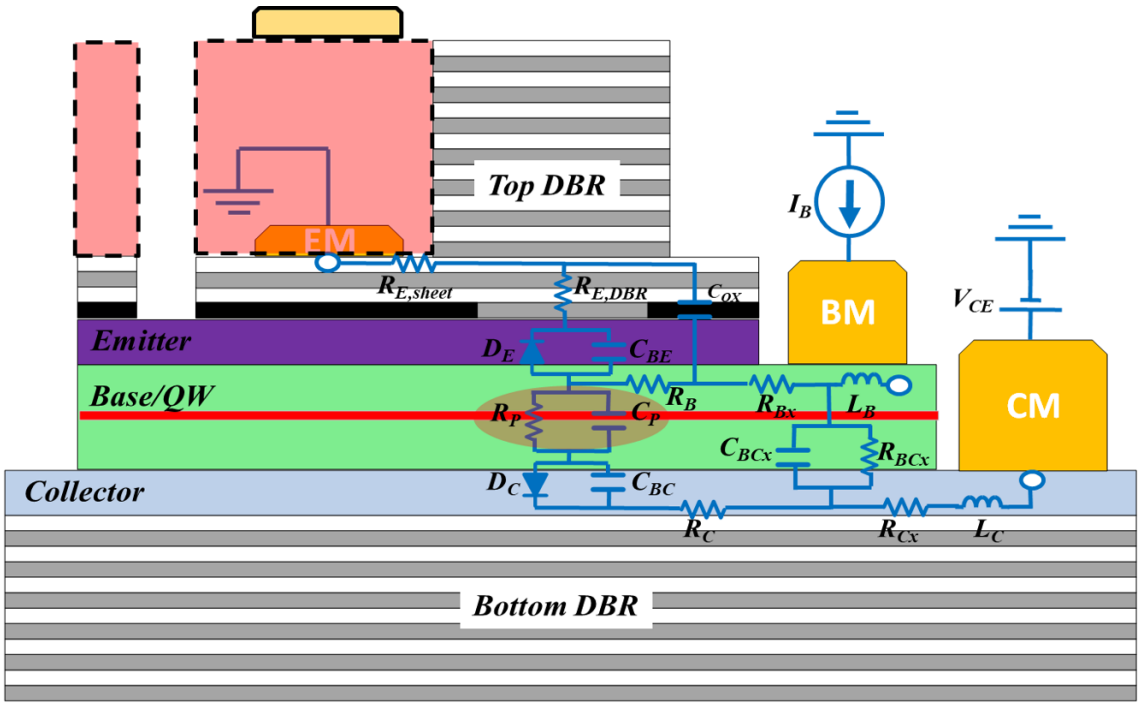

Figure 3.8. Equivalent parasitic circuit of the partially etched VCTL. $R_{E,sheet}$ and $R_{E,DBR}$ are the extrinsic sheet resistance and bulk resistance for emitter current path. D_E and D_C are the intrinsic B-E p-n junction and B-C p-n junction. C_{BE} and C_{BC} are the extrinsic B-E and B-C junction lumped capacitance: depletion and diffusion capacitance. R_P and C_P are the active region photon generation "charging" resistance and capacitance. R_{Bx}, R_{Cx} and R_C are the extrinsic resistance of base and collector. C_{ox}, C_{BCx} and R_{BCx} are the extrinsic leakage capacitance and resistance on the sidewalls. L_B and L_C are the extrinsic signal injection inductance of base and collector ports. The shaded red region is the partially etched region where $R_{E,DBR}$ is greatly reduced.

To illustrate the effect, an equivalent parasitic circuit of the partially etched VCTL is built and shown in Figure 3.8. As shown on the schematic, the emitter resistance that is essentially reduced is the top DBR emitter resistance, $R_{E,DBR}$ by reducing current path

length in the top DBR. Although, an extra term of sheet resistance, $R_{E,sheet}$ (estimated to be ~66 Ω/□ from on wafer TLM measurement), is introduced from the partially etched process, the overall emitter resistance is reduced which can be observed from the electrical I_C-V_{CE} family curves shown in Figure 3.9.

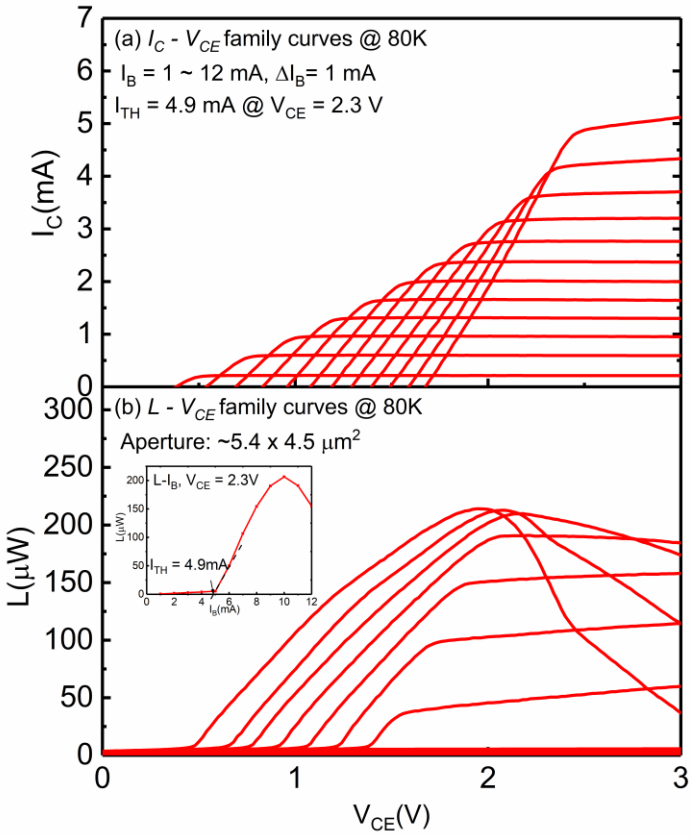

Figure 3.9. (a) collector I_c-V_{CE} and (b) optical L-V_{CE} family characteristic at 80 K. ΔV_{CE} for the measured ΔI_B span, 11 mA, is 1.3 V. This corresponds to a total emitter resistance of 120 Ω. The laser threshold is determined from the L-I_B at a given V_{CE}; I_{TH} = 4.9 mA at V_{CE} = 2.3V as shown in the inset of (b). The maximum light output observed is 220 μW and the optical aperture is determined to be 5.4 × 4.5 μm².

From the I_C-V_{CE} family curves, we observed a ΔV_{CE} = 1.3 V for a ΔI_B span of 11 mA. This corresponds a total emitter resistance, $R_{E,sheet}$ + $R_{E,DBR}$, of 120 Ω. Compared to the previous reported VCTL, which has an estimated emitter resistance of 603 Ω. Since

the bulk resistance of the top DBR is proportional to the current path length, L, the ideal emitter resistance from the partial etch is estimated to be 78 Ω. The difference between the calculated resistance from the ΔV_{CE} and the ideal resistance could be attributed to the growing significance of $R_{E,sheet}$ and the worse contact resistance resulted from the less doped and higher bandgap $Al_{0.12}Ga_{0.88}As$ layer instead of a GaAs contact layer. Nevertheless, the overall emitter resistance is reduced by five folds.

The laser threshold, $I_{B,TH}$, at V_{CE} = 2.3 V is determined to be 4.9 mA from the L-I_B curve, shown in inset of Figure 3.9 (b), and a maximum optical output power of 220 μW is observed. Although the emitter resistance is significantly reduced, the threshold current is twice as high as compared to the previously reported VCTL, $I_{B,TH}$ = 2.4 mA. We have diagnosed the cause of the high threshold to the trench oxidation process, specifically incomplete oxidation sealing beneath the partially etched top mesa and creating a weakly coupled low Q (quality factor) sub-cavity that generates unwanted optical modes. The phenomenon can be seen in the optical spectrum shown in Figure 3.10.

As seen from the optical spectrum of the $5.4 \times 4.5\ \mu m^2$ partially etched VCTL at I_B = 9 mA at V_{CE} = 2.3 V, a weakly coupled spectrum, shown in blue, from the low Q sub-cavity is observed. The sub-cavity has low Q as there are only two pairs of top DBR on top of it and has an aperture of $9.6 \times 8.3\ \mu m^2$ determined from the mode spacings between the fundamental mode and the second order modes. The low Q sub-cavity generates unwanted optical modes that requires additional current injection for photon generation. Hence, a higher laser threshold is needed to support all the optical modes.

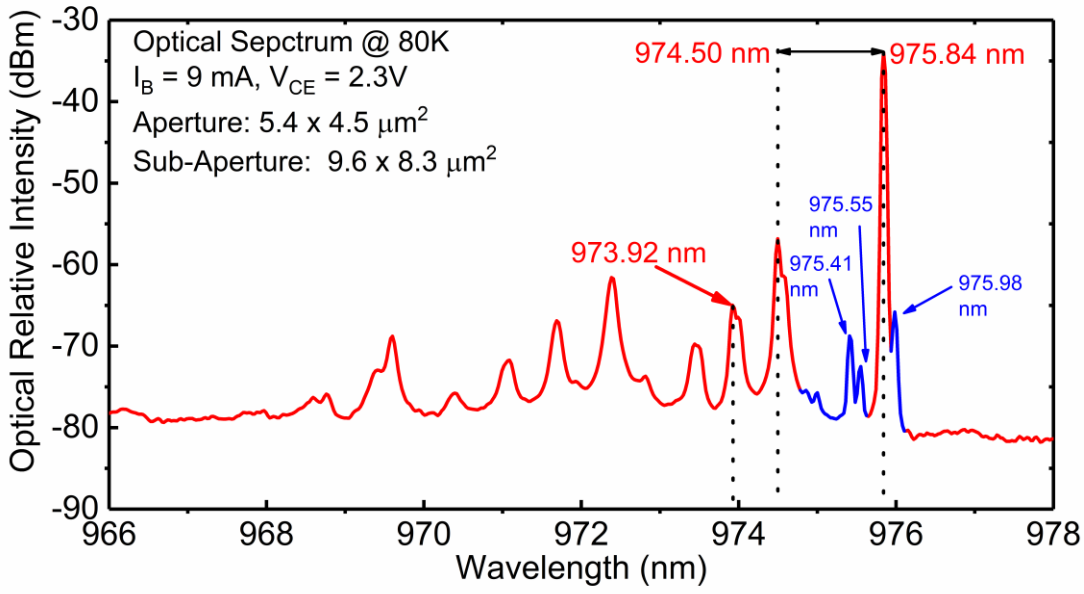

Figure 3.10. The emission spectrum of the 5.4 × 4.5 μm^2 partially etched VCTL at I_B = 9 mA at V_{CE} = 2.3 V. The fundamental mode wavelength, λ(1, 1), is 975.84 nm and a side-mode suppression ratio (SMSR) is observed to be 23 dB. A weakly coupled spectrum, shown in blue, from a low Q sub-cavity with λ(1, 1) = 975.98 nm is observed and an aperture of 9.6 × 8.3 μm^2 is observed.

This phenomenon can be further illustrated by calculating the ideal higher-order transverse modes, e.g. λ(2, 2), λ(3, 1), λ(1, 3) etc., from the high Q cavity with Eqn. 3.3 and match it with the measured spectrum modes. Figure 3.11 shows the spectrum with calculated ideal transverse modes superimposed.

$$\left(\frac{2\pi}{\lambda(m,n)}\right)^2-\left(\frac{2\pi}{\lambda(1,1)}\right)^2=\frac{1}{n}\left[\left(\frac{m^2-1}{a^2}\right)-\left(\frac{n^2-1}{b^2}\right)\right], \tag{3.3}$$

where $\tilde{n}$ = 2.97, a = 5.4 μm, b = 4.5 μm and m and n are the higher mode numbers. In order to achieve low threshold current consistently, the trench oxidation process needs to be optimized to ensure reliable control of oxidation depth to eliminate the low Q sub-cavity.

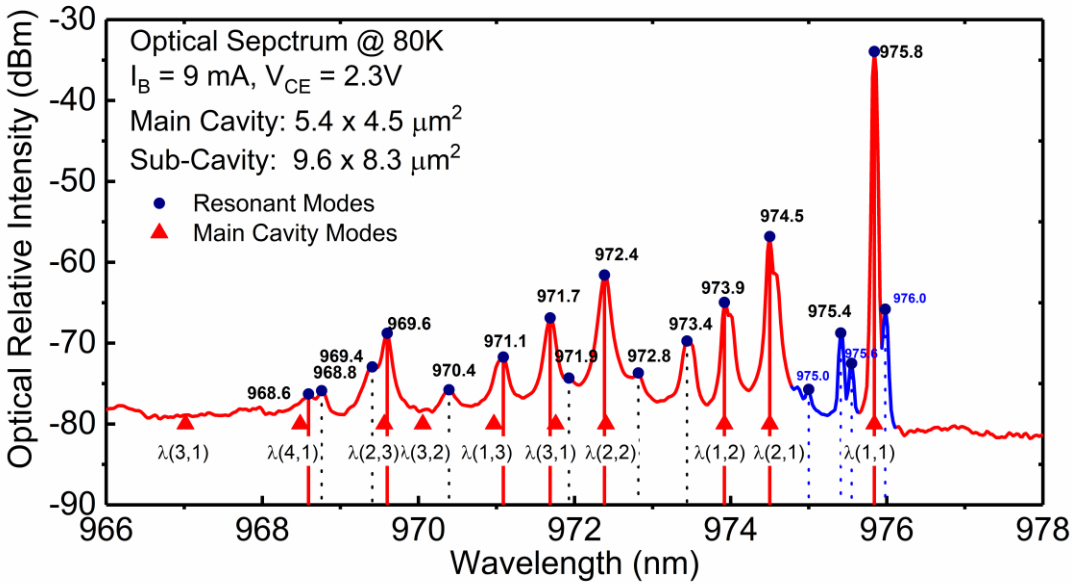

Figure 3.11. Annotated emission spectrum from the same analyzed VCTL with ideal higher transverse modes superimposed (denoted by red triangles). The dropped lines from the major modes match well with the calculated ideal modes. The non-matched peaks could be attributed to the weakly coupled modes from the sub-cavity or hybrid LP modes.

On the electrical side, the low Q sub-cavity potentially is a leakage current path. A modified microwave equivalent circuit of the VCTL is shown in Figure 3.12 to illustrate the effect. We propose that the leakage path introduces resistances, R_{L1} and R_{L2}, capacitances and a mutual inductance, L_M, that is coupled in between the sub-cavity and the main cavity. The capacitances are not specified as they could be potentially lumped with the other parasitic capacitances. To further analyze the effect of the leakage path on the device, the equivalents circuit model is used to fit the measured "cold," I_B = 0 mA and V_{CE} = 0 V, electrical S-parameter data of the presented partially etched VCTL.

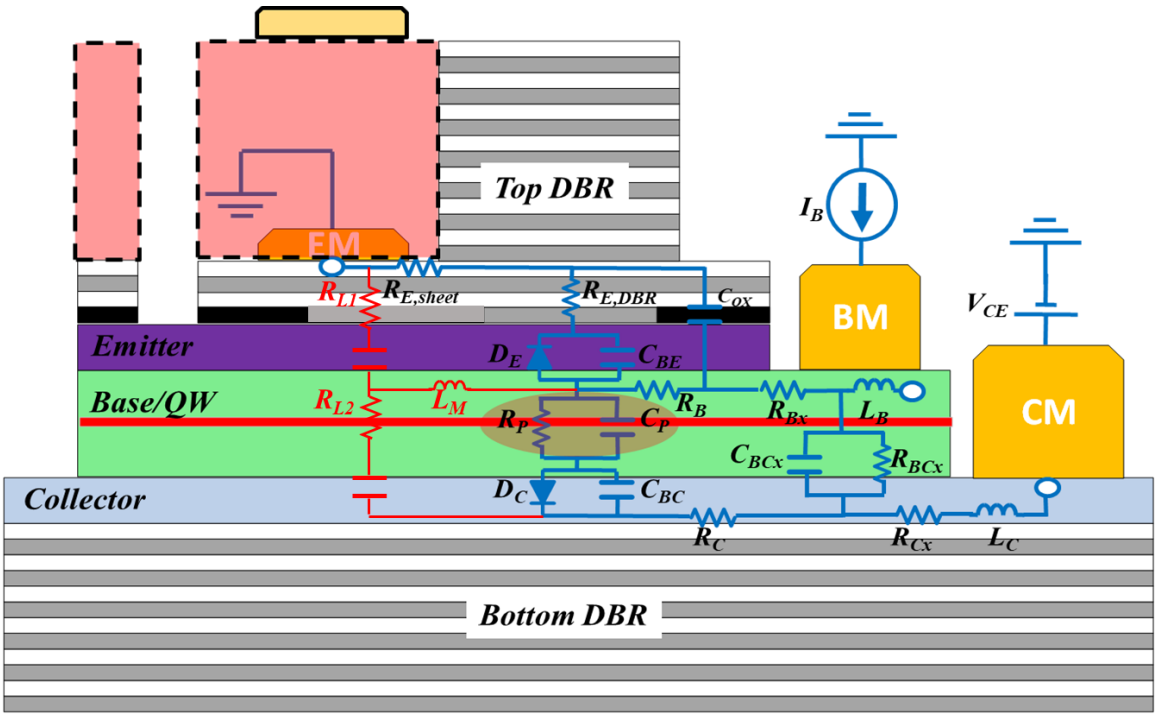

Figure 3.12. Modified microwave equivalent that includes the sub-cavity leakage path shown in red. R_{L1} and R_{L2} are the leakage resistance and L_M is a mutual inductance coupled in between the sub-cavity and the main cavity. The capacitances are not specified as it could be potentially lumped with the other parasitic capacitance.

Figure 3.13 shows the cold measurement data and the fitting results on smith charts in a complex impedance form, $Z = R + jX$ (R is the real part resistance and X is the imaginary part reactance), normalized to a characteristics impedance, Z_o, of 50 Ω. Due to non-optimized RF feed through loss in our cryostat measurement station at high frequency, the high-frequency parts of the measurement data appear to be very noisy, especially on the CE port. Nevertheless, the overall measurement data appears to decent signal-to-noise ration and hence can be justified for parameters fitting purposes.

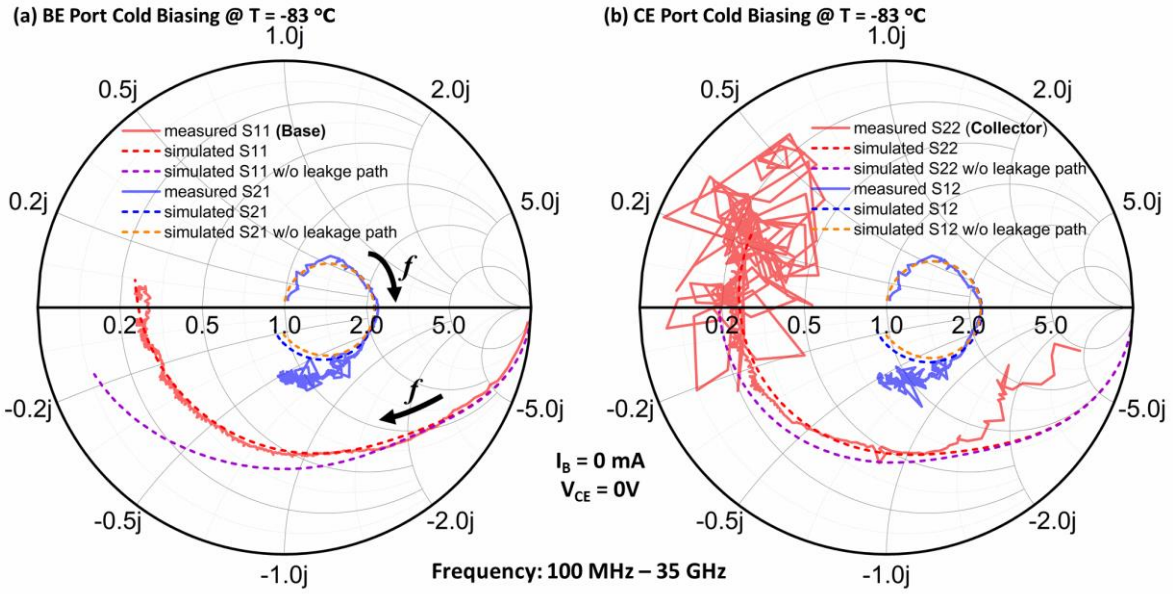

Figure 3.13. Electrical "cold," I_B = 0 and V_{CE} = 0, S-parameter measurements at T = -83 °C (solid line) and simulation (dashed line) of the electrical reflection, S11 & S22, and transmission, S21 & S12, *S*-parameter data between the base and collector of the presented partially etched VCTL. Both with and without leakage path simulation results are shown to illustrate the effect of the leakage path on the electrical side.

To reduce uncertainties in the fitting results, R_E, R_B, R_C, can be calculated from the electrical family and L_B and L_C can be extracted from on-wafer open-short standards. The following expressions outline the parasitic resistance calculation equations and extracted signal injection inductance values:

$$R_E \approx \frac{\Delta V_{CE,offset}}{\Delta I_B}, \tag{3.4}$$

$$R_B \approx \frac{dV_{BE}}{dI_B} - R_E, \tag{3.5}$$

$$R_C \approx \left.\frac{dV_{CE}}{dI_C}\right|_{saturation} - R_E, \tag{3.6}$$

$$L_{B,extracted} = 46\,pH\ , \tag{3.7}$$

and

$$L_{C,extracted} = 44\,pH\ . \tag{3.8}$$

The fitted parameters values are summarized in Table A.2. As shown in Figure 3.13, the simulated results with the leakage path included match the measured data fairly well. From the fitted parameters results, it can be seen that L_C is more than 2 times larger than the extracted value and L_M has a significant value, 170 pH. Also, the leakage path resistances, R_{L1} and R_{L2}, are much smaller than the parasitic resistances. This is expected as the sub-cavity area is about 3 times bigger than the main cavity, where $R \propto 1/A$. Therefore, it is expected a significant amount of injected current flow through the leakage path.

To further illustrate the impact of the inductances and resistance from the leakage path, simulated results without the leakage path are also plotted in Figure 3.13. It becomes apparent that the fitting results do not match well the measurement without the inclusion of the leakage path. Inductance contributes to positive reactance, $j\omega L$, to the complex impedance of the system. On Smith charts, positive reactance corresponds to the top half of the circle. As seen from the electrical reflection, S11 (Base) and S22 (Collector), measurement data at high frequency, there is a non-negligible portion of positive reactance, especially on the collector side. Hence, this indicates there is an exceptionally large L_C as shown from the fitting results. On the Base side, the extracted L_B value matches the fitted value. Nevertheless, the mutual inductance, L_M, has a large impact on the simulated results as "forces" the reactance to be more positive and match the measurement data. As stated,

the resistances, R_{L1} and R_{L2}, are fairly small and do not affect the fitting results as much as the inductances. The electrical transmissions, S12 and S21, are not affected as much as the reflections by the leakage path. Furthermore, the high-frequency components are not fitted well by the equivalent circuit model. Therefore, this suggests the equivalent circuit model needs to be revised and optimized.

Despite having a large laser threshold and an electrical leakage path, a maximum -3 dB modulation bandwidth of 8.5 GHz is observed for the partially etched VCTL. Figure 3.14 (a) and (b) shows the optical frequency response characteristics under direct current modulation, BE port, and voltage modulation, CE port. For the current modulation case under V_{CE} = 2.3V, the highest biasing current is at I_B = 10 mA, which corresponds to I_B/I_{TH} = 2 and a -3 dB bandwidth of 8.5 GHz. The resonance amplitude for each curve is less than 3 dB. Further increase of biasing current drives the VCTL to thermal saturation. Theoretically, if the threshold current can be reduced down through optimizing the trench oxidation process, the same biasing current, I_B = 10 mA, would corresponds to a higher I_B/I_{TH} and hence higher -3 dB bandwidth as shown in Eqns. 3.9 and 3.10:

$$f_{-3dB} \approx 1.55 \cdot \omega_n / 2\pi \,, \tag{3.9}$$

$$\omega_n \propto \sqrt{\frac{1}{\tau_B \tau_{ph}} \left(\frac{I_B}{I_{th}} - 1\right)} \,. \tag{3.10}$$

f_{-3dB} is the laser 3 dB bandwidth, ω_n is the resonance frequency, τ_B is the carrier recombination lifetime, and τ_{ph} is the photon lifetime determined by the cavity design.

For the CE port voltage modulation case, large resonance peaks, ~15 dB, are observed. This directly correlates to the large L_C from the fitting results. We propose that inductance, hence the resonance peak, will be reduced when the trench oxidation process is optimized as a "flat" response has been demonstrated for VCTL [18].

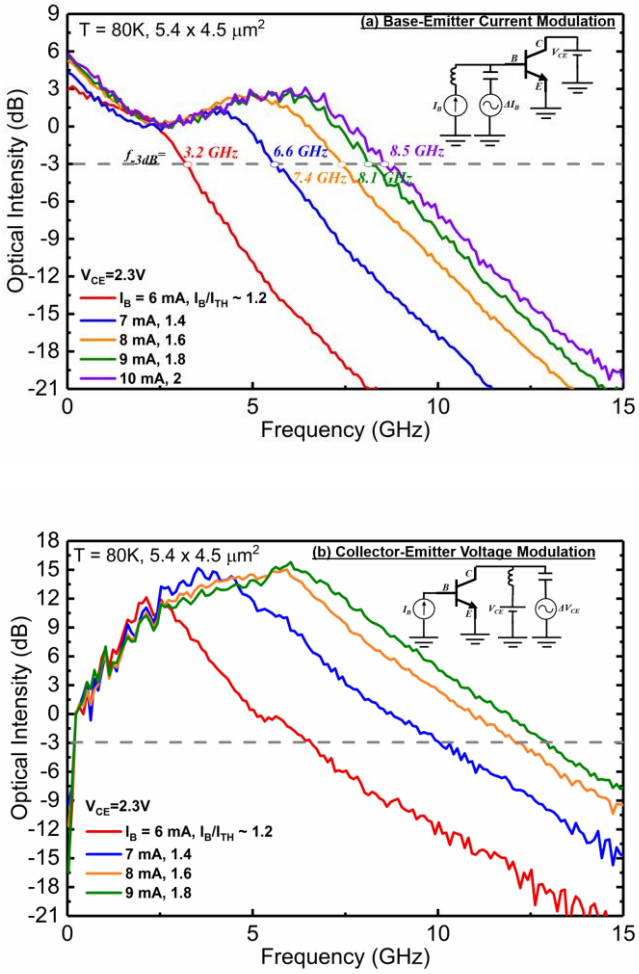

Figure 3.14. Optical frequency response of the partially etched VCTL under (a) direct BE port current modulation and (b) CE port voltage modulation. The circuit schematics shown in the insets depict the modulation scheme for each case. The -3 dB bandwidth of each biasing point for the current modulation case is marked on the curves. The highest measured bandwidth is 8.5 GHz. Large resonance peaks, ~ 15 dB, are observed for all biasing points, which corresponds to the large L_C from the fitting paramters.

It may appear that the bandwidth of the CE port modulation is larger due to the resonance peak; however, the resonance peak is unwanted as it introduces oscillation and degradation of signal integrity in data transmission performance. Therefore, the bandwidth of the CE port modulation is not characterized for this specific lot of partially etched VCTL.

3.4 Summary

In this chapter, we have outlined the development and fabrication process of oxide-confined VCTL. DC and RF characteristics of an oxide-confined VCTL with an optical aperture of $5.4 \times 4.7\ \mu m^2$ is presented. $I_{B,TH}$ and $V_{C,TH}$ are observed for the VCTL due to the photon absorption at the B-C junction. The parasitic emitter resistance is estimated to be 603 Ω by using the Eber-Molls circuit model analysis. A maximum f_{-3dB} of 11.1 GHz is observed for the VCTL with a very low resonance peak despite the large emitter resistance. The emitter resistance of the partially etched VCTL is reduced down to 120 Ω; however, the laser threshold is significantly higher, I_{TH} = 4.9 mA. The origin of the high threshold is attributed to the incomplete trench oxidation, essentially forming a low Q sub-cavity that generates unwanted optical modes. A microwave equivalent circuit is built to characterize the electrical effect of the leakage sub-cavity. The fitting results suggest the sub-cavity is a low resistance path and contributes large inductance to the system. The large threshold sets a thermal limitation on the bandwidth performance; the highest bandwidth measured is only at 8.9 GHz when under BE port modulation. On the other hand, the CE modulation bandwidth shows large resonance peaks, ~ 15 dB, hence further indicating the leakage sub-cavity electrically contributes parasitic inductance.

4. TUNNELING MODULATION IN TRANSISTOR LASER

The base-collector junction of the TL, and VCTL, manifests unique interactions between photons and electrical carriers within the device. The base-collector junction resembles a p-i-n diode and optical absorption in a p-i-n junction diode for a direct-gap semiconductor can be enhanced by photon-assisted tunneling in the presence of a static or dynamic electrical field. In the transistor laser, the coherent photons generated at the base quantum well (QW) interact with the collector field and "assist" optical cavity electron tunneling from the valence band of the base to the conduction band states of the collector. Hence, the intra-cavity photon-assisted tunneling ($IC_{PA}T$) not only affects the light output of the TL but also the carrier distribution in the active base QW region. This $IC_{PA}T$ in a transistor laser is the unique property of voltage (field) modulation and the basis for ultrahigh speed direct laser modulation and switching.

4.1 Intra-Cavity Photon-Assisted Tunneling

The physics of intra-cavity photon-assisted tunneling can be partially explained by the electric field dependent absorption edge of a semiconductor, which often referred to as the Franz-Keldysh effect [42-44]. Optical absorption for a direct-gap semiconductor can be enhanced in the presence of a static electrical field and has been explained as photon-assisted tunneling (PAT) in semiconductor surface and used in a semiconductor PN junction diode [45, 46]. However, previous studies have not included the effect of electro-optical cavity coupling and quality factor, Q. In TL, the coherent photons generated at the base quantum well interact with the collector field and "assist" optical cavity electron

tunneling from the base valence band to the adjacent conduction band of the collector junction.

The energy band diagram and the excess carrier distribution of a TL are shown in Figure 4.1. In addition to the transistor laser base recombination current, I_{r1}, and the base transport current, I_{t1}, the tunneling electrons drift to the collector as an additional current, I_{ICpaT}; also the corresponding tunneling holes drift into the base as a base injection current and then diffuse to the QW for stimulated recombination. Under steady-state operation, the hole current, I_{ICpaT}, is equal to the second base recombination current, I_{r2}. When the excess holes (Δp_2) enter the base, the E-B energy barrier lowers to allow emitter electron injection and via dielectric relaxation transport toward the collector junction on a time scale of a few femtoseconds. For a transistor laser, the base is doped to $\sim 2\times10^{19}\ \mathrm{cm}^{-3}$ and the resistivity calculated to be $\rho \sim\ 4.3\times10^{-3}\ \Omega\cdot\mathrm{cm}$; thus, the dielectric relaxation time is estimated to be $\tau = \varepsilon_r \varepsilon_0 \rho = 4.9$ fs. The excess electrons (Δn_2) correspond to the excess holes (Δp_2) in the base via femtosecond dielectric relaxation transport. The Δn_2 near to the collector junction drifts to the collector and contribute to the second base transport current, I_{t2}. The carriers diffuse toward the QW and contribute I_{r2} to stimulated recombination at the base. This is the operating mechanism of tunneling modulation of a quantum well transistor laser with collector junction tunneling and QW stimulated recombination for tunneling current gain and optical modulation.

The collector current, I_C, can be separated into, I_{C1}, the collector current due to the base QW stimulated recombination and, I_{C2}, the tunneling collector current due to the stimulated optical absorption. Hence, $I_C = I_{C1} + I_{C2}$ and I_{C2} can be expressed as:

$$I_{C2} = I_{t2} + I_{ICPAT}. \tag{4.1}$$

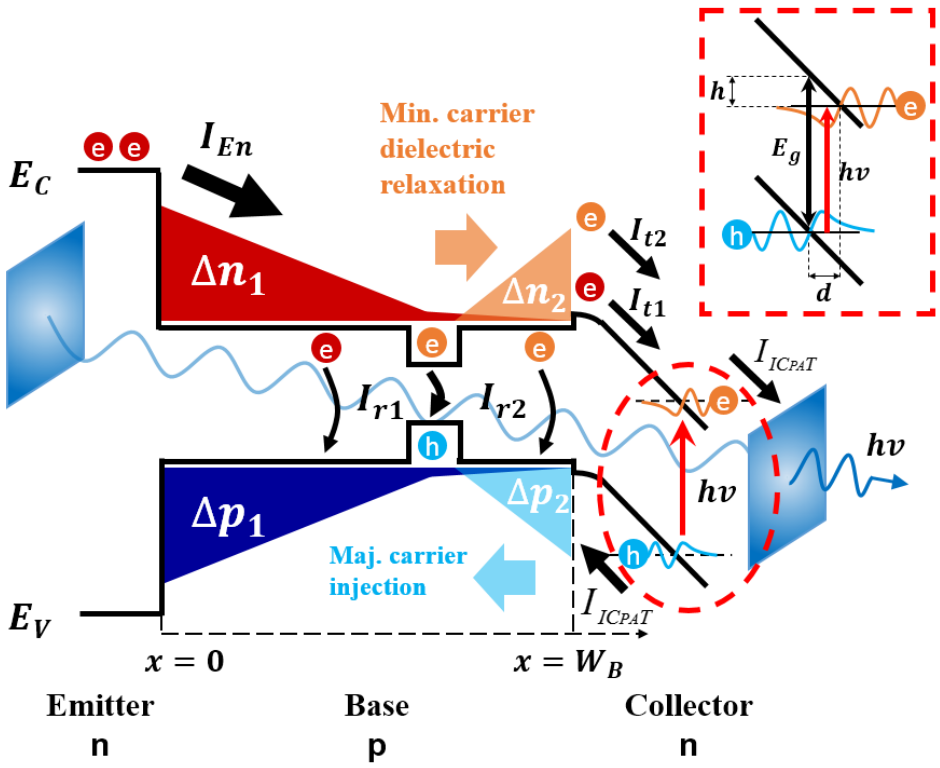

Figure 4.1. Excess carrier distribution in the base of a transistor laser under the influence of tunneling (ICPAT, red circle). Transistor laser operation with emitter current injection, I_{En}, base recombination current, I_{r1}, and base transport and collector drift current, $I_{t1} = I_{C1}$. The intra-cavity photon-assisted electron-hole tunneling at the B-C junction produces the local electron tunneling current, I_{ICPAT}. The tunneling-generated holes accumulate as Δp_2 in the base and thus the corresponding electron, Δn_2, due to dielectric relaxation transport from the emitter toward the collector junction. This leads to the increase of the base transport current, I_{t2}, and the increase of the base recombination current, I_{r2}. The sum of I_{ICPAT} and I_{t2} accounts for the collector current increase of, I_{C2}. The ratio I_{t2}/I_{r2} is the transistor laser tunneling current gain β_2.

The base recombination current, $I_B = I_{r1}$, is often kept constant for a specific biasing point, and the tunneling current equal to base QW stimulated recombination current at steady-state leads to $I_{IC_{PA}T} = I_{r2}$. The transistor laser current gain due to the base recombination without tunneling is defined as $\beta_1 = I_{C1}/I_B \approx I_{t1}/I_{r1}$. A tunneling current gain can be defined as $\beta_2 = I_{t2}/I_{r2}$ to account for the tunneling-induced carrier transport associated with Δn_2 and Δp_2. This leads to

$$I_{C2} = I_{t2} + I_{IC_{PA}T} = I_{t2} + I_{r2} = (\beta_2 + 1) \cdot I_{r2} = (\beta_2 + 1) \cdot I_{IC_{PA}T} . \tag{4.2}$$

Therefore, an increase, or gain, in I_C will result as the result of a corresponding decrease, absorption, of optical output due to $IC_{PA}T$.

To further illustrate the effect of $IC_{PA}T$ on carriers and photon interactions, the I_C-V_{CE} and L-V_{CE} family curves of a common emitter TL is analyzed. A 2 × 200 μm cavity edge emitting TL operating at 20 °C shows the measured outputs of (i) the collector I_C–V_{CE} and (ii) the optical L–V_{CE} family of characteristics in Figure 4.2. The collector I_C-V_{CE} characteristics with a step-upward collector voltage exhibit sharp current changing at switch-UP voltage (V_{TU}) as V_{CE} increases from 0 to 4 V and I_B increases from 0 to 90 mA with steps of ΔI_B = 3 mA. Four different operating regions are identified: (1) the spontaneous region below base current threshold I_{TH} = 43 mA (black, J_{TH} = 10.75 kA/cm^2), (2) laser stimulated region above base current threshold (red), (3) the $I_{IC_{PA}T}$ switch-UP region (blue), and (4) the spontaneous region above base current threshold (I_{TH}) and above collector voltage threshold (V_{TH}) (black). This device shows the unique signature of TL

operation: collector current gain compression at the laser threshold current I_{TH}. This unique characteristic is attributed to the change in base recombination lifetime as the device shifts operation from "slow" spontaneous (black) in region 1 to "faster" stimulated recombination (red) in region 2.

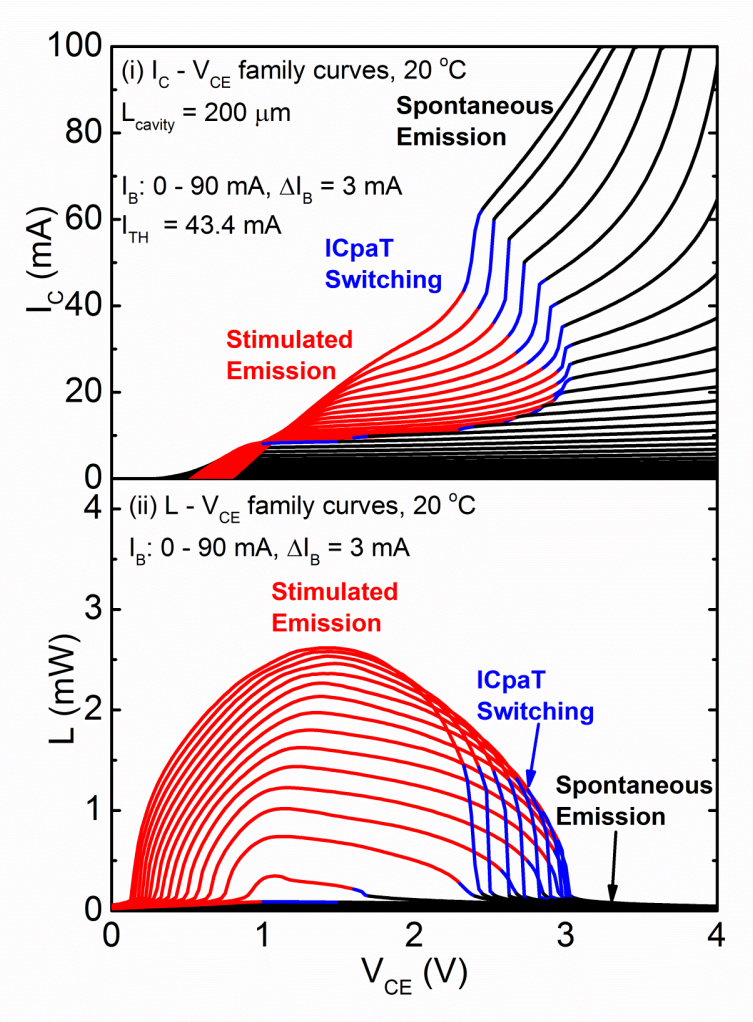

Figure 4.2: A 200 μm transistor laser (i) Collector I_C - V_{CE} and (ii) L –V_{CE} characteristics operating at 20 °C exhibiting a sharp current step-change and different $IC_{PA}T$ voltage switching (blue). Four distinct operating regions are evident: (1) spontaneous recombination below threshold, I_{TH} = 43 mA (black), (2) stimulated recombination and coherent light above threshold (red), (3) collector current and light output switching from stimulated to spontaneous recombination and emission at switch-UP voltages $V_{TU}(I_B)$ (blue), and (4) spontaneous recombination and emission above current threshold and above voltage threshold V_{TU} (black).

The blue region 3 in the I_C-V_{CE} family of characteristics represents electrical switching in the operation due to the base-QW shifting from stimulated to spontaneous recombination. The transistor operates in spontaneous recombination after collector $IC_{PA}T$ switching (black region 4). The blue region in the L-V_{CE} family of characteristics represents optical switching owing to the cavity operation shifting from coherent to incoherent via intra-cavity photon-assisted tunneling. The transistor laser operates in incoherent recombination after collector $IC_{PA}T$ switching, thus, yielding only incoherent light output at low intensity (black region).

4.2 Simultaneous Optical and Electrical Hysteresis Bistability

Optical bistable devices are fundamental to digital photonics as building blocks of switches, logic gates, and memories in future computer systems. Here, we demonstrate both optical and electrical bistability and capability for switching in a single transistor laser operated at room temperature. As shown in Figure 4.2, the $IC_{PA}T$ results in complimentary changes for I_C and L. An electrical current increase corresponds to an optical output decrease and vice versa. For this section, a switch-UP represents a forward V_{CE} sweep with I_C increase and L decrease and a switch-DOWN represents a backward V_{CE} sweep with I_C decrease and L increase.

The physical mechanism of switch-UP is explained by the base-QW shifting operation from stimulate to spontaneous recombination when the optical absorption rate by $IC_{PA}T$ increases with increasing V_{CE} and exceeds the stimulated photon generation rate at the base-QW for a given base current. Subsequently, the cavity photon density drops

below the coherent threshold resulting in switching at switch-UP voltage, V_{TU}. Noticeably, after switching, the transistor is operating under spontaneous but still above laser I_B current threshold, I_{TH}. $IC_{pa}T$ is an ultrafast tunneling process and hence is governed by quantum tunneling time. The quantum tunneling time is characterized as ~ 6 to 8 fs by field emission microscopy [47] and calculated to be ~20 to 50 fs [48]. On the other hand, the mechanism of switch-DOWN is explained by the base-QW shifting operation from spontaneous to stimulated recombination when the optical absorption rate decreases with decreasing V_{CE} and is lower than the spontaneous photon generation rate. Therefore, the cavity photon density can build up from the incoherent state to the coherent threshold through radiative recombination, resulting in switching at switch-DOWN voltage, V_{TD}. Photon generation rate via spontaneous e-h recombination, 10 to 50 ps for HBT-LET [13, 49, 50], is a relatively slower process compared to tunneling. Hence, the electrical and optical hystereses observed for the TL are manifested through the time delay between $IC_{PA}T$ photon reduction and e-h radiative recombination/photon generation in forward and backward switching.

Detailed electrical and optical switching characteristics of the TL at 20 °C and 10 °C are shown in Figure 4.3 (a) and (b). The switch-UP (forward) I_C-V_{CE} and L-V_{CE} family of characteristics (red) in Figure 4.3 a (i) exhibits sharp change at different switch-UP voltages (V_{TU}) as V_{CE} increases from 2 to 3 V and I_B increases from 72 to 90 mA with steps of ΔI_B = 3 mA. For a given I_B = 84 mA (I_{TH} = 43 mA, J_{TH} = 10.75 kA/cm^2), the current difference is ΔI_C = +14 mA and the optical output difference is ΔL = -0.85 mW at V_{TU} = 2.60 V.

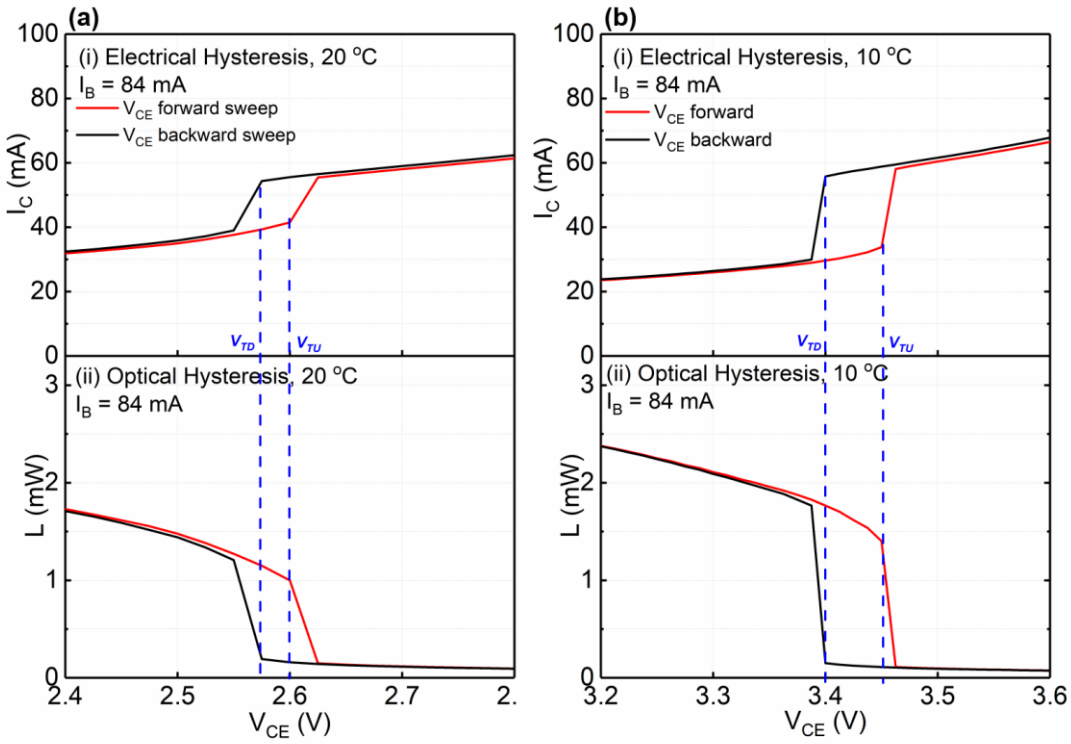

Figure 4.3. Transistor laser electro-optical hysterisis and bistability oprtating at (a) 20 °C and (b) for a given I_B = 84 mA. At 20 °C, the current difference is ΔI_C = 15 mA and the optical light difference is ΔL = 1 mW at V_{TU} (switch-UP) = 2.60 V and V_{TD} (switch-DOWN) = 2.56 V. At 10 °C, the current difference is ΔI_C = 25 mA and the optical light difference is ΔL = 1.5 mW at V_{TU} (switch-UP) = 3.45 V and V_{TD} (switch-DOWN) = 3.4 V.

On the other hand, Figure 4.3 a (ii), when V_{CE} decreases from 3 to 2 V for switch-DOWN (backward) operation, switching at different switch-DOWN voltages (V_{TD}) is exhibited in Figure 4.3 with black. Again, at I_B = 84 mA, the current difference is ΔI_C = -15 mA and the optical output difference is ΔL = +1 mW at V_{TD} = 2.56 V.

When the device is operated at 10 °C and the threshold is reduced to I_{TH} = 33 mA (J_{TH} = 8.25 kA/cm^2), the step-UP family of characteristics (red) in Figure 4.3 b (i) exhibit sharper changes at V_{TU} from 2.5 to 4 V and I_B increases from 69 to 90 mA with steps of ΔI_B = 3 mA. Once again at I_B = 84 mA (I_{TH} = 33 mA), the current difference improves to

ΔI_C = +25 mA and the optical output difference improves to ΔL = -1.5 mW at V_{TU} =3.45 V. When V_{CE} decreases from 4 to 2.5 V for backward operation, different switch-DOWN voltages (V_{TD}) are observed and characteristics (black) are exhibited in Figure 4.3 b (ii). At I_B = 84 mA, the current difference increases to ΔI_C = -25 mA and the optical output difference improves to ΔL = +1.5 mW at V_{TD} = 3.4 V. Due to the difference in switch-UP, V_{TU}, and switch-DOWN, V_{TD}, voltage, the electrical hystereses in the collector I_C-V_{CE} family of characteristics are demonstrated at 20 °C and 10 °C, respectively. Also, the hysteresis loop area increases and switching slope reduces with temperature decreases. Thus, the electrical and optical hysteresis family of characteristics are programmable with base current (I_B), collector voltage (V_{CE}), and the junction temperature.

4.3 Summary

In this chapter, we have established the physics of intra-cavity photon-assisted tunneling, $IC_{PA}T$, in transistor laser. Different from regular photon assisted tunneling, the $IC_{PA}T$ not only influences the optical light output but the carrier distribution, essentially resulting in modulation in the speed of tunneling. The phenomenon is illustrated through the $I_C - V_{CE}$ and $L - V_{CE}$ family of characteristics, where there is a distinct sharp switching, from coherent and incoherent emission, region resulted from $IC_{PA}T$. Furthermore, both electrical and optical bistable hysteresis are observed in TL because of $IC_{PA}T$. The hysteresis results from the time difference between quantum tunneling time, ~fs, and e-h spontaneous recombination in HBT, ~ps. Distinct switch-UP and switch-DOWN voltages

are identified for a wide range of I_B biasing points at both 20 °C and 10 °C. Therefore, we believe $IC_{PA}T$ not only provides ultra-fast tunneling modulation capability but also integration functionality for optical integrated circuits.

5. CONCLUSION AND FUTURE WORK

In this dissertation, we have outlined the development of a microwave technique used to extract the both the extrinsic parasitic and intrinsic parameters of a diode laser. This technique is applied on a high-speed UIUC oxide-confined VCSEL with 5 μm aperture diameter for analysis. The extracted intrinsic modulation bandwidth is 31.86 GHz and 26.19 GHz at RT and 85 °C. Also, the extracted τ_{rec} and τ_p are 0.1778 ns and 4.2 ps at RT and 0.2445 ns and 4.8 ps at 85 °C. With the appropriate terms added to the physical model, the same technique can be applied on TLs. On top of it, we have presented data for an oxide-confined VCTL with an aperture of 5.4 × 4.7 μm^2. Despite having large parasitic emitter resistance of 603 Ω, the VCTL shows an f_{-3dB} of 11.1 GHz. We believe by reducing the emitter resistance, the optical bandwidth would further increase. A fabrication process has been developed to partially etch the top DBR mesa to reduce the emitter resistance.

In terms of high-speed VCTL development and characterization, we have fabricated the partially etched VCTLs. Both DC and RF characteristics are presented. From the analysis on the I_C-V_{CE} family curves, we have successfully reduce the emitter resistance by around 5 folds. However, the threshold current is significantly higher than the previously reported result. The origin of the high threshold current has been attributed to the non-uniform and incomplete trench oxidation process. As a result, a low Q sub-cavity is formed and contributes unwanted optical modes. To further analyze the electrical effect of the sub-cavity, a microwave equivalent circuit model is built to fit the measured electrical S-parameters. From the fitting results, it suggests the sub-cavity is a low resistance leakage path that contributes large parasitic inductance. Nevertheless, a

maximum f_{-3dB} of 8.5 GHz is observed for a 5.4 × 4.5 μm^2 partially etched VCTL. To achieve low threshold and high bandwidth VCTL, the trench oxidation process needs to be optimized and we are currently in the process of doing so.

Intra-cavity photon-assisted tunneling is a newly established physical phenomenon and there are still many aspects of it that need to be investigated. One would be investigating the effect of cavity size or Q, quality factor, has on $IC_{PA}T$. We believe $IC_{PA}T$ is dependent on the photon density in the cavity. The cavity size of edge emitting TL is relatively large, hundreds of μm^2, compared to VCTL, tens of μm^2. Therefore, characterization of small cavity VCTLs is our top priority.

REFERENCES

[1] J. Bardeen and W. H. Brattain, "The transistor, A semi-conductor triode," *Physical Review*, vol. 74, no. 2, pp. 230-231, 07/15/ 1948.

[2] R. N. Hall, G. E. Fenner, J. D. Kingsley, T. J. Soltys, and R. O. Carlson, "Coherent Light Emission From GaAs Junctions," *Physical Review Letters*, vol. 9, no. 9, pp. 366-368, 11/01/ 1962.

[3] N. Holonyak Jr. and S. F. Bevacqua, "Coherent (visible) light emission from $Ga(As_{1-x}P_x)$ junctions," *Applied Physics Letters*, vol. 1, no. 4, pp. 82-83, 1962.

[4] Z. I. Alfërov, V. M. Andreev, D. Z. Garbuzov, Y. V. Zhilyaev, E. P. Morozov, E. L. Portnoy, and V. G. Trofim, "AlAs-GaAs heterojunctions injection lasers with a low room-temperature threshold," *Sov. Phys. Semicond.*, vol. 3, pp. 1107-1110, 1970.

[5] I. Hayashi, M. B. Panish, P. W. Foy, and S. Sumski, "Junction lasers which operate continuously at room temperature," *Applied Physics Letters*, vol. 17, no. 3, pp. 109-111, 1970.

[6] E. A. Rezek, N. Holonyak Jr., B. A. Vojak, G. E. Stillman, J. A. Rossi, D. L. Keune, and J. D. Fairing, "LPE $In_{1-x}Ga_xP_{1-z}As_z$ (x∼0.12, z∼0.26) DH laser with multiple thin-layer (<500 Å) active region," *Applied Physics Letters*, vol. 31, no. 4, pp. 288-290, 1977.

[7] N. Holonyak Jr., R. M. Kolbas, R. D. Dupuis, and P. D. Dapkus, "Room-temperature continuous operation of photopumped MO-CVD $Al_xGa_{1-x}As$-GaAs-$Al_xGa_{1-x}As$ quantum-well lasers," *Applied Physics Letters*, vol. 33, no. 1, pp. 73-75, 1978.

[8] J. M. Dallesasse, N. Holonyak Jr., A. R. Sugg, T. A. Richard, and N. El-Zein, "Hydrolyzation oxidation of $Al_xGa_{1-x}As$-AlAs-GaAs quantum well heterostructures and superlattices," *Applied Physics Letters*, vol. 57, no. 26, pp. 2844-2846, 1990.

[9] N. Holonyak. Jr. and J. M. Dallesasse, "AlGaAs native oxide," U.S. Patent 5262360, 1993.

[10] J. M. Dallesasse and N. Holonyak Jr., "Oxidation of Al-bearing III-V materials: A review of key progress," *Journal of Applied Physics*, vol. 113, no. 5, p. 051101, 2013.

[11] D. R. Scifres and R. D. Burnham, "Distributed feedback diode laser," U.S. Patent 3983509, 1976.

[12] D. L. Huffaker, D. G. Deppe, K. Kumar, and T. J. Rogers, "Native-oxide defined ring contact for low threshold vertical-cavity lasers," *Applied Physics Letters*, vol. 65, no. 1, pp. 97-99, 1994.

[13] M. Feng, N. Holonyak Jr., and W. Hafez, "Light-emitting transistor: Light emission from InGaP/GaAs heterojunction bipolar transistors," *Applied Physics Letters*, vol. 84, no. 1, pp. 151-153, 2004.

[14] G. Walter, N. Holonyak Jr., M. Feng, and R. Chan, "Laser operation of a heterojunction bipolar light-emitting transistor," *Applied Physics Letters*, vol. 85, no. 20, pp. 4768-4770, 2004.

[15] M. Feng, N. Holonyak Jr., G. Walter, and R. Chan, "Room temperature continuous wave operation of a heterojunction bipolar transistor laser," *Applied Physics Letters*, vol. 87, no. 13, p. 131103, 2005.

[16] M. Feng, N. Holonyak Jr., A. James, K. Cimino, G. Walter, and R. Chan, "Carrier lifetime and modulation bandwidth of a quantum well AlGaAs⁄InGaP⁄GaAs⁄InGaAs transistor laser," *Applied Physics Letters*, vol. 89, no. 11, p. 113504, 2006.

[17] M. K. Wu, M. Feng, and N. Holonyak Jr., "surface emission vertical cavity transistor laser," *IEEE Photonics Technology Letters*, vol. 24, no. 15, pp. 1346-1348, 2012.

[18] M. Feng, C.-H. Wu, M. K. Wu, C.-H. Wu, and N. Holonyak Jr., "Resonance-free optical response of a vertical cavity transistor laser," *Applied Physics Letters*, vol. 111, no. 12, p. 121106, 2017.
[19] "Cisco Global Cloud Index: Forecast and Methodology, 2015-2020," *Cisco*, 2015.
[20] D. Mahgerefteh and C. Thompson, "Techno-economic comparison of silicon photonics and multimode VCSELs," presented at the OFC, Los Angeles, CA, 2015.
[21] "The 50 Gbps Si photonics link: A research mileston from Intel Labs," *Intel*.
[22] C. Y. Wang, M. Liu, M. Feng, and N. Holonyak Jr., "Microwave extraction method of radiative recombination and photon lifetimes up to 85 °C on 50 Gb/s oxide-vertical cavity surface emitting laser," *Journal of Applied Physics*, vol. 120, no. 22, p. 223103, 2016.
[23] M. Liu, C. Wang, M. Feng, and N. Holonyak Jr., "Advanced development of 850 nm oxide-confined VCSELs with a 57 Gb/s error-free data transmission," *GOMACTech-2016 (Session 27: Digital Photonics (Paper No. 27.4)*, Thursday 3-17-(2016).
[24] M. Liu, C. Y. Wang, M. Feng, and N. Holonyak Jr., "850 nm oxide-confined VCSELs with 50 Gb/s error-free transmission operating up to 85 °C," Proceedings of the *Conference on Lasers and Electro-Optics*, San Jose, California, 2016/06/05, p. SF1L.6.
[25] P. Westbergh, E. P. Haglund, E. Haglund, R. Safaisini, J. S. Gustavsso, and A. Larsson, "High-speed 850 nm VCSELs operating error free up to 57 Gbit/s," *Electronics Letters*, vol. 49, no. 16, pp. 1021-1023, 2013.
[26] G. Larisch, P. Moser, J. A. Lott, and D. Bimberg, "Impact of photon lifetime on the temperature stability of 50 Gb/s 980 nm VCSELs," *IEEE Photonics Technology Letters*, vol. 28, no. 21, pp. 2327-2330, 2016.
[27] S. Mogg, N. Chitica, U. Christiansson, R. Schatz, P. Sundgren, C. Asplund, and M. Hammar, "Temperature sensitivity of the threshold current of long-wavelength InGaAs-GaAs VCSELs with large gain-cavity detuning," *IEEE J. Quantum Electron.*, vol. 40, no. 5, pp. 453-462, 2004.
[28] C. H. Wu, F. Tan, M. K. Wu, M. Feng, and N. Holonyak Jr., "The effect of microcavity laser recombination lifetime on microwave bandwidth and eye-diagram signal integrity," *Journal of Applied Physics*, vol. 109, no. 5, p. 053112, 2011.
[29] H. Statz and G. deMars, *Quantum Electronics*. New York, N. Y.: Columbia University Press, 1960.
[30] Y. Arakawa, H. Sakaki, M. Nishioka, J. Yoshino, and T. Kamiya, "Recombination lifetime of carriers in GaAs-GaAlAs quantum wells near room temperature," *Applied. Phyics. Letter.*, vol. 46, no. 5, pp. 519-521, 1985.
[31] T. Matsusue and H. Sakaki, "Radiative recombination coefficient of free carriers in GaAs-AlGaAs quantum wells and its dependence on temperature," *Appied Physics Letter*, vol. 50, no. 20, pp. 1429-1431, 1987.
[32] D. D. Sell, H. C. Casey, and K. W. Wecht, "Concentration dependence of the refractive index for n - and p -type GaAs between 1.2 and 1.8 eV," *Journal of Applied Physics*, vol. 45, no. 6, pp. 2650-2657, 1974.
[33] J. Manning, R. Olshansky, and S. Chin, "The carrier-induced index change in AlGaAs and 1.3 um InGaAsP diode lasers," *IEEE Journal of Quantum Electronics*, vol. 19, no. 10, pp. 1525-1530, 1983.
[34] M. Razeghi, *The MOCVD Challenge: A Survey of GaInAsP-InP and GaInAsP-GaAs for Photonic and Electronic Device Applications*. Boca Raton, FL: CRC Press, 2011.
[35] S. B. Healy, E. P. O' Reilly, J. S. Gustavsson, P. Westbergh, Haglund, A. Larsson, and A. Joel, "Active region design for high-speed 850-nm VCSEL," *IEEE J. Quantum Electron.*, vol. 46, no. 4, pp. 506-512, 2010.

[36] G. Walter, C. H. Wu, H. W. Then, M. Feng, and N. Holonyak Jr., "4.3 GHz optical bandwidth light emitting transistor," *Appied Physics Letter,* vol. 94, no. 24, p. 241101, 2009.
[37] M. Feng, H. W. Then, N. Holonyak Jr., G. Walter, and A. James, "Resonance-free frequency response of a semiconductor laser," *Appied Physics Letter,* vol. 95, no. 3, p. 033509, 2009.
[38] F. Tan, R. Bambery, M. Feng, and N. Holonyak Jr., "Transistor laser with simultaneous electrical and optical output at 20 and 40 Gb/s data rate modulation," *Appied Physics Letter,* vol. 99, no. 6, p. 061105, 2011.
[39] R. Bambery, C. Y. Wang, F. Tan, M. Feng, and N. Holonyak Jr., "Single Quantum-Well Transistor Lasers Operating Error-Free at 22 Gb/s," *IEEE Photonics Technology Letters,* vol. 27, no. 6, pp. 600-603, 2015.
[40] H. W. Then, M. Feng, and N. Holonyak Jr., "Microwave circuit model of the three-port transistor laser," *Journal of Applied Physics,* vol. 107, no. 9, p. 094509, 2010.
[41] M. K. Wu, M. Feng, and N. Holonyak Jr., "Voltage modulation of a vertical cavity transistor laser via intra-cavity photon-assisted tunneling," *Applied Physics Letters,* vol. 101, no. 8, p. 081102, 2012.
[42] W. Franz and Z. Naturforsch, *13a,* no. 484, 1958.
[43] L. V. Keldysh, *Sov. Phys.-JETP,* vol. 7, no. 788, 1958.
[44] K. Tharmalingham, *Phys. Rev.*, vol. 130, no. 2204, 1963.
[45] G. E. Stillman and C. M. Wolfe, "Avalanche photodiodes," in *Semiconductors and Semimetals*. vol. 12, ed, 1977, pp. 291-391.
[46] C. M. Wolfe, J. N. Holonyak, and G. E. Stillman, *Physical Properties of Semiconductors*: Prentice Hall, Englewood Cliffs, NJ, 1989.
[47] S. K. Sekatskii and V. S. Letokhov, "Electron tunneling time measurement by field-emission microscopy," *Physical Review B,* vol. 64, no. 23, p. 233311, 11/27/ 2001.
[48] Z. S. Wang, L. C. Kwek, C. H. Lai, and C. H. Oh, "Quantum tunneling time," *Physical Review A,* vol. 69, no. 5, p. 052108, 05/14/ 2004.
[49] H. W. Then, M. Feng, N. Holonyak Jr., and C. H. Wu, "Experimental determination of the effective minority carrier lifetime in the operation of a quantum-well n-p-n heterojunction bipolar light-emitting transistor of varying base quantum-well design and doping," *Appied Physics Letter,* vol. 91, no. 3, p. 033505, 2007.
[50] G. Walter, C. H. Wu, H. W. Then, M. Feng, and N. Holonyak Jr., "Tilted-charge high speed (7 GHz) light emitting diode," *Appied Physics Letter,* vol. 94, no. 23, p. 231125, 2009.

APPENDIX A: TABLES

TABLE A.1 Electrical Parasitic Parameters of High-Speed Oxide-Confined VCSEL

Table A.1. Electrical Parasitic Parameters of High-Speed 5 μm Aperture Oxide-Confined VCSEL

RT	I (mA)	C_p (fF)	R_p (Ω)	$R_{m,n} + R_{m,p}$ (Ω)	dV/dI (Ω)	C_a (fF)	C_{diff} (fF)	R_j (Ω)	$f_{-3dB, overall}$ (GHz)	$f_{-3dB,intrinsic}$ (GHz)
I_{TH} = 0.8 mA	1.6	106	11.3	111	133	98	332.57	34	11.09	11.97
	2.4	103	11.1	99	108.4	98	372	26	15.11	16.07
	3.2	102	11	92	94.6	98	422	20	17.81	19.03
	4.8	97	11.1	83.5	77.4	98	512	12.3	21.91	22.96
	12	88	10.6	63.9	51	98	812	6.5	29.15	31.86
85 ˚C	I (mA)	C_p (fF)	R_p (Ω)	$R_{m,n} + R_{m,p}$ (Ω)	dV/dI (Ω)	C_a (fF)	C_{diff} (fF)	R_j (Ω)	$f_{-3dB, overall}$ (GHz)	$f_{-3dB,intrinsic}$ (GHz)
I_{TH} = 1.08 mA	2	96	12	85	101.4	98	502	22	11.79	12.4
	2.4	95	11.9	82	94.5	98	522	19	13.8	14.58
	3.6	91	11.7	75.5	81.7	98	562	14	17.99	18.86
	5.5	88	11.2	69	70.6	98	632	10.3	21.74	22.44
	9.6	84	10.3	61	59.3	98	772	7.5	24.53	26.19

TABLE A.2 Electrical Parasitic of the Presented Partially Etched VCTL

Table A. 2. Electrical Parasitic and Leakage Path Parameters of the Presented Partially Etched VCTL

Resistance (Ω)	Capacitance (fF)	Inductance (pH)	Leakage Path
R_E* = 120	C_{BE} = 90	L_E = 0	L_M = 170 pH
R_B = 14	C_{BEx} = 155	L_B = 46	R_{L1} = 14 Ω
R_{Bx} = 6	C_{BC} = 400	L_C = 102	R_{L2} = 2 Ω
R_C = 110	C_{BCx} = 86		
R_{Cx} = 8.8			

R_E* = $R_{E,sheet}$ + $R_{E,bulk}$